

## Graphical Abstract

**Coaxial multi-criteria optimization of a methane steam reforming reactor for effective hydrogen production and thermal management**

Marcin Pajak, Grzegorz Brus, Janusz S. Szmyd

## Highlights

### **Coaxial multi-criteria optimization of a methane steam reforming reactor for effective hydrogen production and thermal management**

Marcin Pajak, Grzegorz Brus, Janusz S. Szmyd

- Introduction of a novel approach to the macro-patterning concept.
- Sensitivity analysis conducted for the evolutionary algorithm parameters.
- Enhancement of thermal conditions via a modification of the catalyst insert.
- Increase in hydrogen productivity.

# Coaxial multi-criteria optimization of a methane steam reforming reactor for effective hydrogen production and thermal management

Marcin Pajak<sup>a,\*</sup>, Grzegorz Brus<sup>a</sup>, Janusz S. Szmyd<sup>a</sup>

<sup>a</sup>*AGH University of Science and Technology, Krakow, Poland*

---

## Abstract

The advancement in environmental awareness is the recent driving factor of the energy industry development. The market sentiments dictate the commercialization of unconventional energy sources. Thus, generation via hydrogen conversion gains popularity. The presented research regards the enhancement of the steam reforming reaction, used for the production of hydrogen via the conversion of hydrocarbons. The reforming process characterizes by a strong endothermic nature. The rapid course of the reaction leads to the creation of temperature gradients of a considerable magnitude. The presented research strives to alleviate the negative consequences of the reaction character. An original strategy by the name of macro-patterning is suggested as a remedy. The presented research proposes an updated concept, predicting the introduction of coaxial segments to the catalytic insert. The segments may consist of catalytic material or metallic foam applied for local suppression of the reaction. The morphology of specific segments may be altered independently, to allow for additional control of the reforming reaction. The objective of the research is to define the optimal segment composition. The optimization process is based on an in-house procedure implementing a genetic algorithm. The acquired results appear to validate the macro-patterning concept. A significant unification of the temperature field is obtained, with a simultaneous increase in hydrogen productivity.

*Keywords:* hydrogen, evolutionary algorithms, reforming, design optimization

---

\*Corresponding author

Email address: [mpajak@agh.edu.pl](mailto:mpajak@agh.edu.pl) (Marcin Pajak)

---

## 1. Introduction

Hydrogen technologies are one of the promising directions of the clean energy sector development [1]. The research on hydrogen is conducted to provide a reliable alternative to the currently dominant fossil fuel energy sources [2, 3]. Hydrogen might be used as an energy carrier for internal combustion or fuel cells, both resulting in steam being the main product [4, 5]. However, with the application of hydrogen technology, some crucial issues arise. The first issue regards hydrogen acquisition, as it does not occur on Earth in its pure form. The second matter is hydrogen storage, with currently no effective measures of long-term storage [6, 7]. The two most common processes for on-the-spot production of hydrogen are water electrolysis and the reforming of hydrocarbons [8, 9]. Water electrolysis is a process predicting the breaking of chemical bonds between oxygen and hydrogen in particles of water. The current state of the electrolysis development is far from meeting economical requirements [10]. The only reasonable use of water electrolysis is to deplete surplus energy generated from renewable sources during low market demand and short-term storage of hydrogen for further use during increased demand for energy [11]. The second measure for hydrogen production is the reforming reaction [12, 13]. The reforming process is a catalytic reaction used for the conversion of hydrocarbons for the production of hydrogen [14, 15]. The reforming process can be successfully applied to the conversion of biofuels, allowing the reforming process to be considered a renewable hydrogen source [16, 17]. Furthermore, the process can be successfully applied as a measure of carbohydrate-based waste gases or plastic recycling, establishing it as a prominent for hydrogen generation [18, 19]. The reforming technology brings a series of issues regarding the thermal conditions occurring inside the reactor. The strong endothermic nature of the process results in the occurrence of thermal stresses and may lead to a shortening of the reactor's lifespan [20]. The presented research aims to reduce the drawbacks of the process, by enhancement of the thermal conditions. The majority of researchers focused on the parametric study and optimization of the reaction conditions, resulting in improvements only to a certain extent [21, 22]. Further development of the process is pursued by the introduction of new materials and design concepts, including new catalyst structures [23, 24], the introduction of new kinds of catalyst supports [25], or by rethinking the

design of the reactor itself [26, 27, 28]. A captivating opportunity is described in a work by Palma et al. [29], who introduced a structured catalyst for the intensification of the reforming reaction. The research confirms the improvement of the reaction rate, resulting from the enhancement of the axial and radial temperature distribution. The research reported by Yun et al. [30] focuses on the enhancement of heat transfer, by modification of the design, to acquire a maximized heat transfer area. The proper handling of heat in the reforming process is confirmed to enhance the overall process conduction [31]. Furthermore, a rapid temperature decay at the upstream region of the reactor results in thermal stresses forming in the reactor. Thus, leading to its uneven degradation and reduction of the unit's lifetime [32]. A unification of the temperature distribution may not only improve the conditions but also achieve easier control of the process [33]. The presented research aims to alleviate the negative consequences of the strong endothermic character of the process, via the introduction of radial division of the catalytic insert. The concept originates from the approach proposed by Settar et al. [34]. The research predicted an introduction of macro-patterned active surfaces with an introduction of metallic foam matrices, focusing on providing advantageous thermal conditions for the reaction [35, 36]. The presented research extends the concept to fill the whole reactor's volume with a catalytic composite of nickel and yttria-stabilized zirconia (Ni/YSZ), to maximize the reaction region in the reactor. Further, the reforming unit is divided into segments in the radial direction, instead of the longitudinal division [37]. Non-catalytic metallic foam is used as a substitute for parts of the catalyst, to adjust the intensity of the reaction proceeding, leading to the unification of the thermal field inside the reactor. To define the optimal alignment of the catalyst, an evolutionary algorithm is coupled with an in-house reforming simulation [38]. The presented analysis includes:

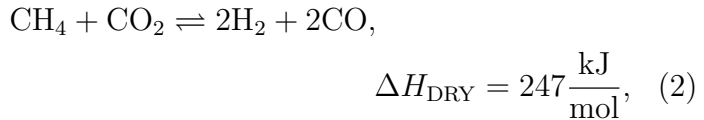
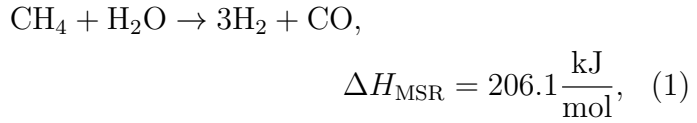
- Investigation of the macro-patterning concept applicability with the introduction of the catalytic insert radial division.
- Introduction of two separate principles for the configuration of the segments.
- Comprehensive sensitivity analysis to define the finest performing set of the evolutionary algorithm parameters.
- Analysis of the results robustness, via measuring the hydrogen productivity of specimens defined by the specific algorithms.

## 2. Mathematical model

The reactor geometry is designed to allow modification of the insert in a real-life scenario. The analyzed process incorporates a plug-flow reactor, maintaining axial symmetry throughout its whole volume. The reactor consists of a straight, cylindrical pipe, allowing for an accessible replacement of the catalyst insert when required. The introduced macro-patterning strategy predicts modification of the catalyst insert's morphology and its partial substitution with a non-catalytic material. Substitution of the catalyst material serves to enhance the heat transfer inside the reactor [37]. Metallic foams are chosen for application to the indicated issues [39]. To provide a relevant measure for altering the temperature distribution inside the reactor, the catalyst insert is divided into segments. Each segment may consist of a catalyst or a non-catalytic material, with their morphological parameters individually assigned. The insert's segmentation is carried out according to two separate strategies. The first strategy predicts division in the radial direction with maintaining a constant width of inlet surfaces of each cylinder (Fig. 1 b)). The second strategy predicts the application of segments with an identical area of the inlet surfaces for each of the coaxial cylinders (Fig. 1 c)). The design is prepared to contain exclusively simple geometrical shapes, allowing to maintain an insignificant computational complexity of the domain [40].

### 2.1. Chemical Reactions Model

The process is assumed to be dominated by three reactions, as reported in literature [41, 42, 33]. The reactions are steam reforming of methane (MSR) (Eq. (1)), dry reforming of methane (DRY) (Eq. (2)), and water-gas shift reaction (WGS) (Eq. (3)) [43]. The stoichiometric equations for the reactions are presented below:



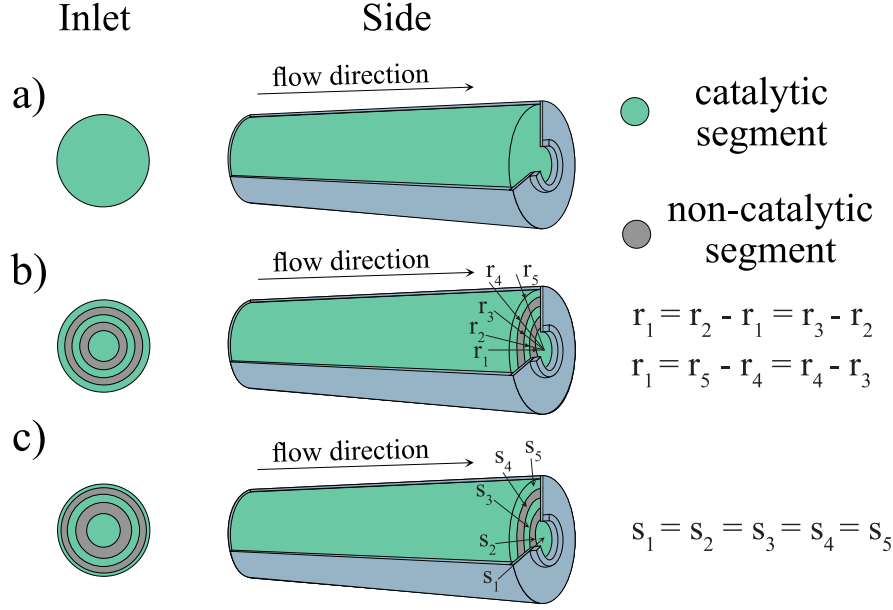
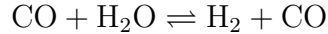


Figure 1: The investigated macro-patterning designs: a) conventional reactor with homogeneous and continuous catalytic insert, b) catalytic insert divided in the radial direction (equal width of inlet surface), c) catalytic insert divided in the radial direction (equal area of inlet surface)



$$\Delta H_{\text{WGS}} = -41.15 \frac{\text{kJ}}{\text{mol}}. \quad (3)$$

The reformer is supplied with a mixture of  $\text{H}_2$ ,  $\text{CO}_2$ , and  $\text{CH}_4$ . The composition of the feedstock is determined by the steam-to-carbon ratio ( $SC$ ) parameter, defining the ratio of steam to methane provided at the reactor's inlet. The process conditions are remarkably influenced by the  $SC$  value, as the reactions' rates depend directly on the composition of the inlet gases [44]. A proper setting of the  $SC$  is crucial for the prevention of the carbon deposition phenomenon [45]. Adverse process conditions can result in carbon particles precipitating on the catalyst surface [46]. A proper setting of the ratios and the process' temperature are proven to have the most significant influence on the alleviation of the poisoning hazard [47]. The enthalpy changes  $\Delta H$  are taken from literature [37, 48]. Knowledge of their rates is

essential to allow the inclusion of the reactions into the model. According to the research conducted by Brus et al. [49], the effective rate of MSR and DRY reactions can be expressed with a common equation:

$$R_{\text{eff}} = \dot{w}_{\text{cat}} A_{\text{MSR}} \exp \left( -\frac{E_a}{\bar{R}T} \right) p_{\text{CH}_4}^\alpha (p_{\text{H}_2\text{O}} + p_{\text{CO}_2})^\beta. \quad (4)$$

The individual reaction rates for the MSR and DRY reactions can be distinguished as follows:

$$R_{\text{MSR}} = R_{\text{eff}} \frac{p_{\text{H}_2\text{O}}}{p_{\text{CO}_2} + p_{\text{H}_2\text{O}}}, \quad (5)$$

$$R_{\text{DRY}} = R_{\text{eff}} \frac{p_{\text{CO}_2}}{p_{\text{CO}_2} + p_{\text{H}_2\text{O}}}. \quad (6)$$

The reforming reaction is reported to occur rather slowly [50]. However, the WGS reaction has a more unpredictable nature [51]. Thus, the preparation of a formula, returning proper values regardless of the process conditions, is not feasible. According to Ahmed and Föger, the WGS reaction can be assumed to maintain equilibrium under specific conditions [52]. The equilibrium assumption has been successfully applied in other numerical analyses [53, 54, 55]. The assumption also meets a good agreement between the calculations and the experimental data [56, 57, 58]. Taking into account the provided literature review, the WGS reaction is assumed to be in the equilibrium state in the presented analysis. The process conditions are designed to satisfy the equilibrium assumption. Following the statements, CO, CO<sub>2</sub>, H<sub>2</sub> and H<sub>2</sub>O have to satisfy the equilibrium equation, expressed by the following formula:

$$K_{\text{WGS}} = \frac{k_{\text{WGS}}^+}{k_{\text{WGS}}^-} = \frac{p_{\text{CO}_2} p_{\text{H}_2}}{p_{\text{CO}} p_{\text{H}_2\text{O}}} = \exp \left( -\frac{\Delta G_{\text{WGS}}^0}{\bar{R}T} \right). \quad (7)$$

The WGS reaction rate can be further expressed using Eq. (8):

$$R_{\text{WGS}} = k_{\text{WGS}}^+ p_{\text{CO}} p_{\text{H}_2\text{O}} + k_{\text{WGS}}^- p_{\text{H}_2} p_{\text{CO}_2}. \quad (8)$$

The value of  $R_{\text{WGS}}$  can be acquired through the analysis of the reforming process stoichiometry and balancing the chemical species [59, 60]. Balancing the reaction's stoichiometry allows for the calculation of the partial pressures

included in Eq. (7), leading to the relation describing the WGS reactions' rate (Eq. (9)) [49].

$$R_{\text{WGS}} = \frac{n_{\text{CH}_4}^{\text{outlet}}}{V} = \frac{n_{\text{CH}_4}^{\text{inlet}} \cdot xcr}{V} ycr. \quad (9)$$

Following, the methane conversion rate  $xcr$  and carbon monoxide conversion rate  $ycr$  can be specified with:

$$xcr = 1 - \frac{n_{\text{CH}_4}^{\text{inlet}} - R_{\text{MSR}}V}{n_{\text{CH}_4}^{\text{inlet}}}, \quad (10)$$

$$ycr = \frac{K_{\text{WGS}} + 3xcr - \sqrt{\chi - \omega}}{2(K_{\text{WGS}} - 1)}, \quad (11)$$

where:

$$\chi = (K_{\text{WGS}}SC + 3xcr)^2, \quad (12)$$

$$\omega = 4K_{\text{WGS}}xcr(K_{\text{WGS}} - 1)(SC - xcr). \quad (13)$$

Coupling Eq. (10) with Eq. (9) and applying simple mathematical transformations results in the formulation of a final expression for the WGS reaction's rate:

$$R_{\text{WGS}} = R_{\text{MSR}}ycr. \quad (14)$$

The mass consumption and production rates of the reforming process reactions (Eqs. (1) - (3)), are summarized in the Table 1. The values are further applied to the mass transfer equation (Eq. (19)), as a part of its source terms. The heat generation rates by the described reactions are calculated depending on the rates of the reactions (Eqs. (5), (6), (14)) and the values of enthalpy change  $\Delta H$  [41, 49]. The heat generation rates are given below:

$$Q_{\text{MSR}} = -\Delta H_{\text{MSR}}R_{\text{MSR}}, \quad (15)$$

$$Q_{\text{DRY}} = -\Delta H_{\text{DRY}}R_{\text{DRY}}, \quad (16)$$

$$Q_{\text{WGS}} = -\Delta H_{\text{WGS}}R_{\text{WGS}}. \quad (17)$$

## 2.2. Heat and Mass Transfer Model

The fundamental transport equations are incorporated into the mathematical model. Considering the computational domain defined for the needs of the analysis, the equations are implemented for two dimensions. Therefore, the model's equations are solved along the axis and radius of the reactor's geometry. The volume-averaging method was chosen for the derivation of the governing equations implemented in the model used for this analysis. The process parameters are locally averaged for each representative volume and included in the mathematical formulas [61]. Values of continuity (Eq. (18)), mass transfer (Eq. (19)), momentum (Eqs. (21) and (22)) and energy equations (Eq. (27)) characterize the transport phenomena occurring during the reforming process. The equations are derived for the laminar flow. The analyzed fluids are considered to be Newtonian and incompressible. Thus, the continuity equation takes the following form [62, 63]:

$$\frac{\partial(\rho_0 U_x)}{\partial x} + \frac{1}{r} \frac{\partial(r\rho_0 U_r)}{\partial r} = 0, \quad (18)$$

The species conservation is calculated using molar fractions of species taking part in the reaction (Equation (19)). The formulated equation is derived from Fick's law of diffusion [33]. The mass sources and sinks  $S_j$  depend on the MSR, DRY, and WGS rates and molar masses of the species taking part in the reaction [20, 64]. The exact equations defining the values of  $S_j$  are described in Table 1.

$$\begin{aligned} \rho_0 \left( U_x \frac{\partial Y_j}{\partial x} + U_r \frac{\partial Y_j}{\partial r} \right) &= \frac{\partial}{\partial x} \left( \rho_0 D_{j,\text{eff}} \frac{\partial Y_j}{\partial x} \right) \\ &+ \frac{1}{r} \frac{\partial}{\partial r} \left( r \rho_0 D_{j,\text{eff}} \frac{\partial Y_j}{\partial r} \right) + S_j. \end{aligned} \quad (19)$$

The effective mass diffusivity of species  $D_{j,\text{eff}}$  was calculated using the equation explained below (Eq. (20)) [65]:

$$D_{j,\text{eff}} = (1 - \sqrt{1 - \varepsilon}) D_j. \quad (20)$$

The diffusion of substance  $j$  in the gas mixture  $D_j$  is computed using Fuller's method and Blanc's law. The gases' properties are taken from the literature [66]. The values assumed for the flow model describe the local phase

Table 1: Mass sources/sinks

species	mass generation MSR	mass generation WGS	mass generation DRY	summarized generation
H <sub>2</sub>	$3R_{\text{MSR}}M_{\text{H}_2}$	$R_{\text{WGS}}M_{\text{H}_2}$	$2R_{\text{DRY}}M_{\text{H}_2}$	$3R_{\text{MSR}}M_{\text{H}_2} + R_{\text{WGS}}M_{\text{H}_2} + 2R_{\text{DRY}}M_{\text{H}_2}$
CO	$R_{\text{MSR}}M_{\text{CO}}$	$-R_{\text{WGS}}M_{\text{CO}}$	$2R_{\text{DRY}}M_{\text{CO}}$	$R_{\text{MSR}}M_{\text{CO}} - R_{\text{WGS}}M_{\text{CO}} + 2R_{\text{DRY}}M_{\text{CO}}$
CO <sub>2</sub>	0	$R_{\text{WGS}}M_{\text{CO}_2}$	$-R_{\text{DRY}}M_{\text{CO}_2}$	$R_{\text{WGS}}M_{\text{CO}_2} - 2R_{\text{DRY}}M_{\text{H}_2}$
CH <sub>4</sub>	$-R_{\text{MSR}}M_{\text{CH}_4}$	0	$-R_{\text{DRY}}M_{\text{H}_2}$	$-R_{\text{MSR}}M_{\text{CH}_4} - R_{\text{DRY}}M_{\text{H}_2}$
H <sub>2</sub> O	$-R_{\text{MSR}}M_{\text{H}_2\text{O}}$	$-R_{\text{WGS}}M_{\text{H}_2\text{O}}$	0	$-R_{\text{MSR}}M_{\text{H}_2\text{O}} - R_{\text{WGS}}M_{\text{H}_2\text{O}}$

average of the gas control volume. The momentum conservation depends directly on the insert's morphology. The materials composing the insert are considered porous. Therefore, parameters describing the material structure have to be included in the equations. The parameters are porosity  $\varepsilon$ , permeability  $K_p$ , and inertial coefficient  $c_{\text{ine}}$  [38]. A separate momentum equation is formulated for each of the computational domain dimensions (Eqs. (21) and (22)).

$$\frac{\rho_0}{\varepsilon_0^2} \left( U_x \frac{\partial U_x}{\partial x} + U_r \frac{\partial U_x}{\partial r} \right) = -\frac{\partial P}{\partial x} + \frac{\mu}{\varepsilon} \left[ \frac{\partial^2 U_x}{\partial x^2} + \frac{1}{r} \frac{\partial}{\partial r} \left( r \frac{\partial U_x}{\partial r} \right) \right] - \frac{\mu}{K_p} U_x - \frac{\rho_0 c_{\text{ine}}}{\sqrt{K_p}} U_x \sqrt{U_x^2 + U_r^2}, \quad (21)$$

$$\frac{\rho_0}{\varepsilon_0^2} \left( U_x \frac{\partial U_r}{\partial x} + U_r \frac{\partial U_r}{\partial r} \right) = -\frac{\partial P}{\partial r} + \frac{\mu}{\varepsilon} \left[ \frac{\partial^2 U_r}{\partial r^2} + \frac{1}{r} \frac{\partial}{\partial r} \left( r \frac{\partial U_r}{\partial r} \right) - \frac{U_r}{r^2} \right] - \frac{\mu}{K_p} U_r - \frac{\rho_0 c_{\text{ine}}}{\sqrt{K_p}} U_r \sqrt{U_x^2 + U_r^2}. \quad (22)$$

The permeability  $K_p$  of the specific segment is calculated using (23), basing on the information about its porosity  $\varepsilon$  [67]:

$$K_p = \frac{\varepsilon(1 - (1 - \varepsilon)^{1/3})}{36((1 - \varepsilon)^{1/3} - (1 - \varepsilon))} d_p^2, \quad (23)$$

where  $d_p$  stands for an average pore diameter. The inertial coefficient  $c_{\text{ine}}$  was calculated using [68]:

$$c_{\text{ine}} = 0.0095 g_s^{-0.8} \sqrt{\frac{\varepsilon}{3(\tau - 1)}} (1.18 \sqrt{\frac{(1 - \varepsilon)}{3\pi}} \frac{1}{g_s})^{-1}, \quad (24)$$

where tortuosity  $\tau$  and shape function  $g_s$  are expressed with following equations [67, 68]:

$$\tau = \frac{\varepsilon}{1 - (1 - \varepsilon)^{1/3}}, \quad (25)$$

$$g_s = 1 - \exp(-\frac{1 - \varepsilon}{0.04}). \quad (26)$$

The energy conservation equation (Eq. (27)) describes the process of heat transfer during the reaction. The equation includes local thermal conditions, the materials' parameters, and the heat sources calculated using Eqs. (15) - (17).

$$\rho_0 C_p \left( U_x \frac{\partial T_{\text{loc}}}{\partial x} + U_r \frac{\partial T_{\text{loc}}}{\partial r} \right) = \frac{\partial}{\partial x} \left( \lambda_{\text{eff}} \frac{\partial T_{\text{loc}}}{\partial x} \right) + \frac{1}{r} \frac{\partial}{\partial r} \left( r \lambda_{\text{eff}} \frac{\partial T_{\text{loc}}}{\partial r} \right) + Q_s. \quad (27)$$

Due to the application of metallic foam, a proper relation describing the  $\lambda_{\text{eff}}$  of the material is essential [68]. The model chosen for calculating the value of the  $\lambda_{\text{eff}}$  was proposed by Boomsma and Poulikakos and further corrected by Dai et al. [69, 70]. The outcome relation allows for the derivation of equations describing the thermal conductivity of metallic foams. According to the literature review, an adequate model including the morphology of metallic foams is prepared [71].

$$\lambda_{\text{eff}} = \frac{\sqrt{2}l}{2(R_A + R_B + R_C + R_D)}, \quad (28)$$

where  $R_A$  -  $R_D$  stand for the thermal resistances of the porous media cell subsections [37, 70].

### 3. Numerical model

To solve systems of the defined equations a discretization of the previously prepared continuous computational domain is necessary. The numerical model is prepared using the Finite Volume Method [72]. A uniform computational grid with evenly spaced nodes is formed, to assure a minimal complexity of the calculations, [40]. The grid's dimensions are established at 150 elements in the longitudinal and 25 elements in the radial directions, resulting in square-shaped elements. A single grid sector is presented in Fig. 2

#### 3.1. Transport Equations

Integration of the fundamental transport equations of the reforming process over the created control volumes is conducted [73]. The partial differential equations covering the species conservation (Eq. (19)), the momentum

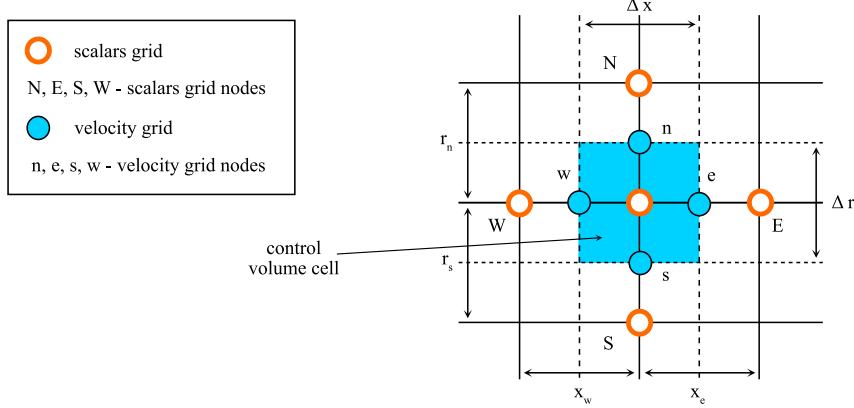


Figure 2: Numerical grid implemented in the analysis

conservation equation (Eqs. (21) - (22)), and the energy conservation equation (Eq. (27)) may be described in a generalized form [73], as follows:

$$\Psi_x \frac{\partial \phi}{\partial x} + \Psi_r \frac{\partial \phi}{\partial r} = \frac{\partial}{\partial x} \left( \Gamma \frac{\partial \phi}{\partial x} \right) + \frac{1}{r} \frac{\partial}{\partial r} \left( r \Gamma \frac{\partial \phi}{\partial r} \right) + \bar{S}. \quad (29)$$

The Eq. (29) is prepared to allow substitution of any dependant variable  $\phi$ . The coefficients on the left side of the Eq. (29),  $\Psi_x$  and  $\Psi_r$ , describe the convective terms in  $x$  and  $r$  directions and may be substituted accordingly to the use case. The diffusive terms, represented by  $\Gamma$ , are placed on the right-hand side of the equation, along with the source terms  $\bar{S}$ . The corresponding terms and coefficients are summarized in Tab. 2. The source terms  $\bar{S}$  values regard the catalytic segments only. The reaction is assumed to be put to a halt for the non-catalytic region of the insert. Therefore, no heat and mass production nor consumption is predicted for the metallic foam segments.

### 3.2. Coaxial segments configuration

The reactor has been divided into five concentric segments, constituting four hollow cylinders and a core. The segments may take one of two configurations. The first one predicts equal width of the inlet and outlet surfaces, while the second configuration predicts an equal area of inlet and outlet surfaces. The two possible setups are summarized in Fig. 3.

Table 2: Coefficients and terms for substitution in Eq. (29)

Eq.	$\phi$	$\Psi_x$	$\Psi_r$	$\Gamma$	$\bar{S}$
(19)	$Y_j$	$\rho_0 U_x$	$\rho_0 U_r$	$\rho_0 D_{j,\text{eff}}$	$S_j$
(21)	$U_x$	$\frac{\rho_0}{\varepsilon_0^2} U_x$	$\frac{\rho_0}{\varepsilon_0^2} U_r$	$\frac{\mu}{\varepsilon_0}$	$-\frac{\partial P}{\partial x} - \frac{\mu}{K_p} U_x - \frac{\rho_0 c_{\text{ine}}}{\sqrt{K_p}} U_x \sqrt{U_x^2 + U_r^2}$
(22)	$U_r$	$\frac{\rho_0}{\varepsilon_0^2} U_r$	$\frac{\rho_0}{\varepsilon_0^2} U_r$	$\frac{\mu}{\varepsilon_0}$	$-\frac{\partial P}{\partial r} - \frac{\mu}{K_p} U_r - \frac{\rho_0 c_{\text{ine}}}{\sqrt{K_p}} U_r \sqrt{U_x^2 + U_r^2} - \frac{\mu U_r}{\varepsilon_0 r^2}$
(27)	$T$	$\rho_0 C_p U_x$	$\rho_0 C_p U_r$	$\lambda_{\text{eff}}$	$Q_s$

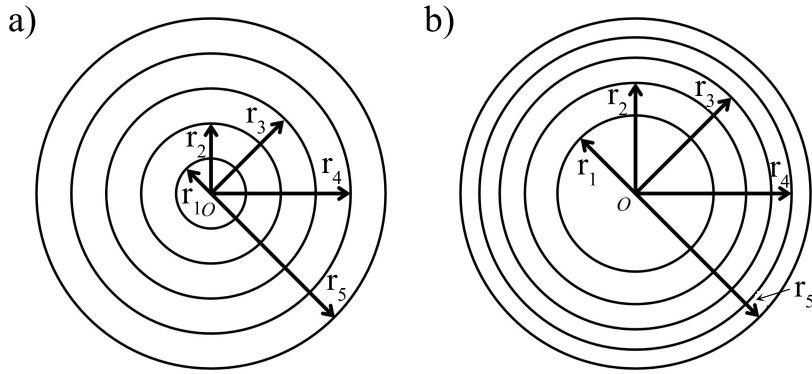


Figure 3: The coaxial segments configurations: a) equal width of rings, b) equal inlet and outlet surface

The exact dimensions of the particular rings for Fig. 3 b) are calculated using the system of equations (30), as follows:

$$\begin{cases} 2\pi r_1^2 = \frac{2}{5}\pi R^2 \\ 2\pi (r_2^2 - r_1^2) = \frac{2}{5}\pi R^2 \\ 2\pi (r_3^2 - r_2^2) = \frac{2}{5}\pi R^2 \\ 2\pi (r_4^2 - r_3^2) = \frac{2}{5}\pi R^2 \\ 2\pi (r_5^2 - r_4^2) = \frac{2}{5}\pi R^2 \end{cases} \quad (30)$$

The values resulting from solving the Eqs. (30) are presented in Tab. 3.

The computational domain is indicated with the red dashed line (Fig. 4). Segments can be described with the following parameters - porosity, average

Table 3: Rings' dimensions

Radius	Equal width (cm)	Equal surface (cm)
$r_1$	1	$\sqrt{5}$
$r_2$	2	$\sqrt{10}$
$r_3$	3	$\sqrt{15}$
$r_4$	4	$2\sqrt{5}$
$r_5$	5	5

pore size, as well as their catalytic properties, which are directly correlated to the porosity value. The analyzed model is steady and the flow of gases is assumed to be laminar and occurring in one direction. Fluids taking part in the process are assumed to be Newtonian. The presented numerical analysis is a quasi-three-dimensional case. Due to the axial symmetry of the reactor's tube, a computational domain can be constrained to a two-dimensional cross-section of the reformer. Implementation of proper boundary conditions allows assuming the process occurs in the same manner throughout the reactor's whole volume [73].

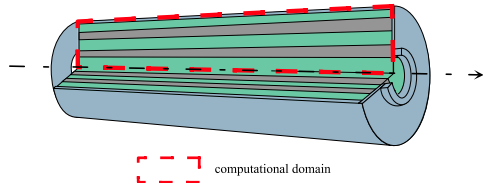


Figure 4: Quasi 3-dimensional computational domains for the rings configurations

### 3.3. Boundary Conditions and Materials

To complete the preparation of the numerical analysis, setting the properties of the materials and the boundary conditions is vital. Proper setting of  $SC$  value is essential for this analysis, due to the threat of carbon deposit formation [74]. If the ratios are chosen incorrectly, the carbon deposition phenomenon may occur, poisoning the reactor's catalyst [75]. Choosing an appropriate steam-to-carbon ratio allows for avoiding the described hazard.

The value of  $SC$  for this analysis was set to be equal to 2.0 [-], preventing this occurrence [43, 47]. The catalyst insert's segments are assumed to consist of one of two materials. The first material is a catalytic composite of nickel and yttria-stabilized-zirconia (Ni/YSZ). The second material, serving the purpose of heat transport medium, is chosen to be steel foam. The metallic foam segments are introduced for the unification of the temperature distribution inside the reactor. Suppression of the reforming reaction, combined with a considerable heat exchange surface for foams, is expected to let the gases mixture reheat effectively [76]. The value of  $\lambda_{\text{solid}}$  is set at  $22 \text{ W m}^{-1} \text{ K}^{-1}$  for the catalytic material [77], while the value of  $\lambda_{\text{solid}}$  for the steel foam is established at  $30 \text{ W m}^{-1} \text{ K}^{-1}$  [78]. The dimensionless cubic node length  $e$  is set to be equal to 0.0339, as explained by Boomsma and Poulikakos [69]. The temperature of the fuel flowing inside the unit is considered to reach the temperature of the reformer instantly. The symmetry boundary conditions are set at the symmetry axis, while the no-slip boundary condition is applied at the wall of the reformer. The boundary conditions necessary for the solution of the governing equations are summarized below.

#### *Thermal Boundary Conditions*

- inlet temperature  $T = T_{\text{in}} = 900 \text{ K}$  at  $x = 0$  and  $0 \leq r < R$ ,
- outlet temperature  $\partial T / \partial x = 0$  at  $x = L$  and  $0 \leq r < R$ ,
- symmetry boundary condition  $\partial T / \partial r = 0$  at  $0 \leq x < L$  and  $r = 0$ ,
- wall heat flux  $\partial T / \partial r = \text{const}$  at  $0 \leq x < L$  and  $r = R$ .

The thermal boundary condition set at the reactor's wall is chosen to be of a second type. Constant heat flux is assumed on the reactor's wall, and the wall itself is the medium for heat exchange between the reactor and the system boundaries. The wall thickness is set to be equal to 0.001 m and is assumed to consist of the same material as the metallic foams. Thus, the value of  $\lambda_{\text{solid}}$  for the reactor's wall is equal to  $30 \text{ W m}^{-1} \text{ K}^{-1}$  [78]. The boundary conditions essential for the calculation of the species conservation equations are presented below.

#### *Mass Transport Boundary Conditions*

- inlet mole fractions  $Y_j = Y_{j,\text{in}}$  at  $x = 0$  and  $0 \leq r < R$ ,

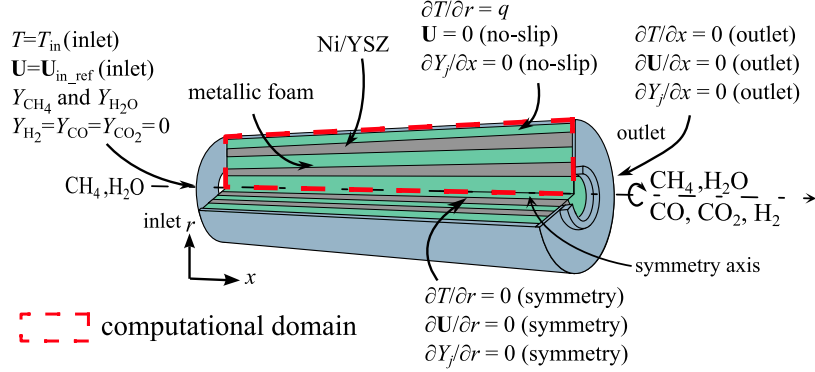


Figure 5: Boundary conditions applied in the analysis

- outlet mole fractions  $\partial Y_j / \partial x = 0$  at  $x = L$  and  $0 \leq r < R$ ,
- symmetry boundary condition  $\partial Y_j / \partial r = 0$  at  $0 \leq x < L$  and  $r = 0$ ,
- no-slip boundary condition  $Y_j = 0$  at  $0 \leq x < L$  and  $r = R$ .

To complete the numerical model's setting, the boundary conditions for solving the momentum conservation equations are needed. The conditions are applied in the manner listed below.

#### *Momentum Boundary Conditions*

- inlet velocity  $U = U_{in} = 0.15 \text{ m s}^{-1}$  at  $x = 0$  and  $0 \leq r < R$ ,
- outlet velocity  $\partial U / \partial x = 0$  at  $x = L$  and  $0 \leq r < R$ ,
- symmetry boundary condition  $\partial U / \partial r = 0$  at  $0 \leq x < L$  and  $r = 0$ ,
- no-slip boundary condition  $U = 0$  at  $0 \leq x < L$  and  $r = R$ .

All of the boundary conditions are summarized in Fig. 5.

## 4. Genetic algorithm

The conducted optimization includes the application of an evolutionary algorithm, to define the optimal design of the catalytic insert for the coaxial segments. The genetic algorithm (GA) is selected to be the optimization procedure used for the needs of the analysis. The algorithm analyses subsequent,

finite populations of test specimens, which parameters are inherited from the specimens acquiring the best results in the preceding generation. The results are evaluated by user-defined fitness functions [79]. The functions are exclusive to a certain problem. If more than one function is defined, the functions have to be combined into a single value, which will be further processed by the genetic algorithm itself [80]. The remaining part of the genetic algorithm operation is the mutation procedure. The mutation is used as an additional procedure for preventing the local extremum trap and a measure for the introduction of genes that were not present in the initial population or are just not possible to acquire on the way of the crossover procedure [81]. Coupling of the prepared numerical analysis with the algorithm requires proper parametrization of reactor parameters [80]. The catalyst insert is set to contain 5 coaxial segments. Each of the segments is assumed to consist of either a catalytic composite of nickel with yttria-stabilized-zirconia (Ni/YSZ) or a stainless steel foam [71]. The insert regions may differ in their morphological parameters regardless of the constituting material. The parameters altered by the algorithm are segment catalytic character, porosity  $\varepsilon$  and average pore diameter  $d_p$ . The porosity values available for application in the analysis are constrained to the range between 0.5 and 0.8. The lower boundary is set at 0.5, as lower porosity values resulted in over-significant pressure drops during the preliminary calculations. The choice of 0.8 as the upper boundary is motivated by lower accessibility to the manufacturing methods determined for metallic foams of higher porosities [82]. The average pore diameters  $d_p$  are calculated for each segment, based on the values of the porosity [71]. The upper boundary of the  $d_p$  range is restricted by the model conditions. According to the volume-averaging method, the size of a single pore is not allowed to exceed the size of a single numerical grid element. Therefore, the upper boundary is limited to 0.002 m [61]. Furthermore, segment porosity  $\varepsilon$  has a direct influence on the catalyst density. The catalyst density  $\dot{w}_{\text{cat}}$  is calculated using Eq. (31):

$$\dot{w}_{\text{cat}} = \rho_{\text{cat}} \cdot (1 - \varepsilon_0), \quad (31)$$

where  $\rho_{\text{cat}}$  is equal to  $5.3448 \cdot 10^6 \text{ g m}^{-3}$ . The chemical reaction kinetics model derived for the implemented numerical simulation regards a Ni/YSZ composite with a 60:40 Ni to YSZ ratio [71]. Nickel serves the catalytic purpose, while YSZ serves as a scaffold. Therefore, the basic catalyst density for the Ni/YSZ element should be calculated concerning the ratio of the

materials. The solid nickel density equals to  $8.908 \cdot 10^6$  g m<sup>-3</sup> [83]. The value of  $\rho_{\text{cat}}$  is calculated by applying the given ratio to the value of the solid nickel density [71]. The definition of the relations allows commencing the operation of the GA. The algorithm starts its operation with the preparation of the initial generation, with the specimens' parameters fully randomized. First, the segments' character is randomized. The algorithm is expected to generate catalytic and non-catalytic segments in a ratio of 50:50, as the randomization procedure uses a uniform distribution for its seed [84]. When the specific segment's character is determined, the algorithm randomizes its porosity  $\varepsilon$  and average pore size  $d_p$  values. As the final initialization step, the GA calculates the catalyst density for each of the segments designated to consist of Ni/YSZ composite. Having defined the initial parameters, the reforming simulation code is executed for each of the generated reactors. The overall operation of the algorithm prepared for the needs of the research is presented in Fig. 6.

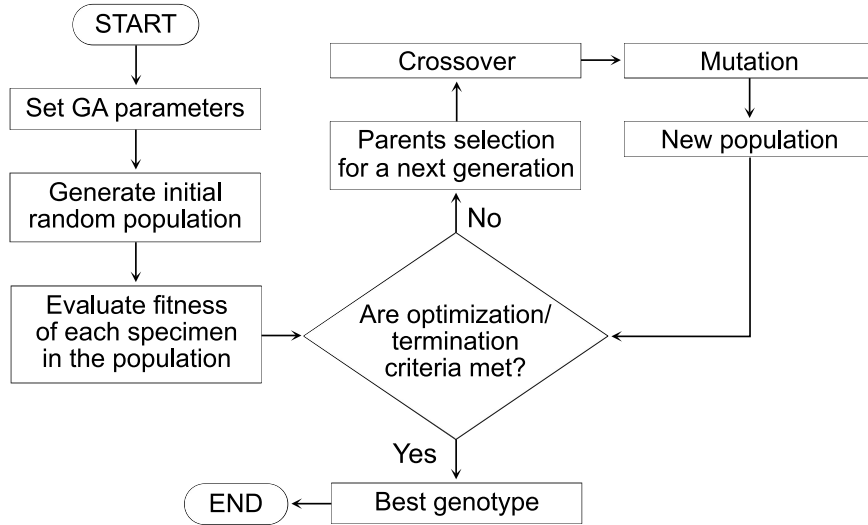


Figure 6: Summary of the genetic algorithm procedure

The conducted investigation regards optimization of the temperature field distribution inside the reactor, simultaneously maintaining a considerable methane conversion rate [38]. Therefore, the research is considered a multi-objective optimization, as the fitness analysis is required to investigate two separate factors. The first factor is temperature distribution. The main objective is to reduce the temperature gradients occurring throughout the

reactor's volume during the reaction. The strong endothermic character of the process has a consequence in large temperature decreases in the regions in which the fuel concentration is significant. The constant transition of the temperature field leads to the establishment of thermal stresses, leading to premature degradation of the catalyst material [85]. The presented research predicts the search for an optimal distribution of catalytic and non-catalytic segments and proper selection of their porosity  $\varepsilon$  and average pore size  $d_p$ . The first function  $f_{CH_4}$  regards the methane conversion rate. The fuel conversion rate is calculated using the molar fractions of the methane at the inlet and the outlet of a specific reactor. The  $f_{CH_4}$  value is calculated using Eq. (32):

$$f_{CH_4} = \frac{(frac{CH_4}_{in} - frac{CH_4}_{out})}{frac{CH_4}_{in}}, \quad (32)$$

The remaining fitness function  $f_T$  evaluates the extent of the unification of the temperature distribution inside the catalytic insert. Essentially, the thermal fitness objective is to find the  $\Delta T$  value, being a representative temperature difference for a specific reactor. To assure reliability and accuracy of the mathematical formula, the thermal fitness is established to perform the temperature distribution analysis for each of the grid elements separately [38]. The algorithm iterates through each of the created control volumes and calculates the temperature difference between the central node  $T_P$  and each of the neighboring control volumes  $T_N$ ,  $T_E$ ,  $T_S$ ,  $T_W$  (Fig. 7). Further, each of the control volumes has its specific temperature difference  $\Delta T_{loc_{i,j}}$  assigned. The  $\Delta T_{loc_{i,j}}$  value is chosen to be the highest temperature difference among the values calculated for each of the neighboring control volumes. The  $\Delta T_{loc_{i,j}}$  for each of the cells is based on the following formula:

$$\begin{aligned} \Delta T_{loc_{i,j}} = \\ \max \{ |T_{P_{i,j}} - T_{N_{i,j}}|, |T_{P_{i,j}} - T_{E_{i,j}}|, |T_{P_{i,j}} - T_{S_{i,j}}|, |T_{P_{i,j}} - T_{W_{i,j}}| \}. \end{aligned} \quad (33)$$

Having computed the set of the  $\Delta T_{loc_{i,j}}$  for the whole numerical grid, the algorithm selects the highest value among computed  $\Delta T_{loc_{i,j}}$  and saves it as a global  $\Delta T$  value representing a specific reactor (Eq. (34)).

$$\Delta T = \max \{ T_{loc_{1,1}}, T_{loc_{1,2}}, \dots, T_{loc_{i,j}} \}, \quad (34)$$

where  $i$  and  $j$  indices represent the numerical grid's dimensions. The final thermal fitness value  $f_T$  is computed using the following formula:

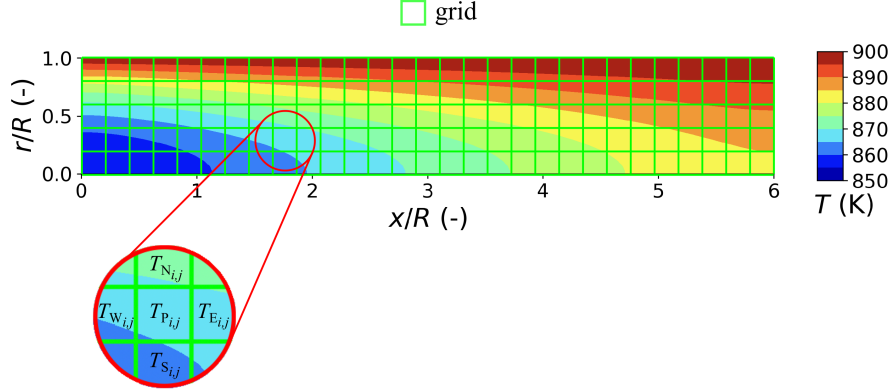


Figure 7: Temperature field evaluation strategy

$$f_T = 1 - \frac{\Delta T}{\Delta T_{\max}}, \quad (35)$$

where  $\Delta T_{\max}$  stands for the highest temperature difference value reported for a single generation. The acquired  $f_{\text{CH}_4}$  and  $f_T$  values are further combined into a single fitness value  $f$ , using the weighted-sum method [86]:

$$f = \sum_{i=1}^N w_i f_i. \quad (36)$$

where  $N$  represents the number of the specimens. The weights  $w_i$  are established at 0.2, 0.4, 0.5, 0.6, and 0.8. Each of the analyses being carried out applied each of the weights to both of the fitness functions to allow the conduction of a sensitivity analysis, depending on the assumed importance of the defined fitness functions. The conducted numerical investigation includes a search for an optimal arrangement of coaxial segments, simultaneously performing a sensitivity analysis of the weights applied for the fitness calculation.

## 5. Numerical analysis

The presented investigation regards the optimization of the temperature distribution inside the reforming reactor. Moderation of the temperature field is achieved via the introduction of the macro-patterning concept [37]. The concept predicts the modification of the catalytic insert of a reforming reactor, resulting in a change in the process conditions. The insert is divided into segments in the radial direction. Each segment may consist of catalytic Ni/YSZ or stainless steel foam. The algorithm conducts the search for an optimal composition of the insert, altering the percentage of the catalyst used, segments placement, and segments structural parameters. The metallic foam is introduced to suppress the reforming reaction. A sensitivity analysis is conducted to specify the most suitable multiplication factors for the weighted-sum fitness calculation (Eq. (36)) [87]. The computed fitness is used to rank the specimens in a single genetic algorithm's iteration. An analysis of the genetic algorithm behavior, depending on the weight applied to the two fitness functions is conducted, to define the most suitable approach to the issue, depending on the applied variant of the macro-patterning strategy. The analysis includes a comparison of results for five different sets of fitness weights, as follows:

1.  $w_{\text{CH}_4} = 0.2, w_T = 0.8$
2.  $w_{\text{CH}_4} = 0.4, w_T = 0.6$
3.  $w_{\text{CH}_4} = 0.5, w_T = 0.5$
4.  $w_{\text{CH}_4} = 0.6, w_T = 0.4$
5.  $w_{\text{CH}_4} = 0.8, w_T = 0.2$

The analysis has to be preceded by a definition of a reference case. A comparison of subsequent optimization results with the reference case will serve as a benchmark for defining if any significant improvement in the reaction conditions has been noted for a specific case. The reference case defined for the presented analysis is a conventional reforming reactor, with a catalytic insert being homogeneous and continuous throughout the whole volume of the reactor. The whole insert consists of a composite of nickel and yttrium-stabilized-zirconia (Ni/YSZ) with a ratio of 60:40. The porosity  $\varepsilon$  of the reactor's catalyst is set at 50 %, resulting in the catalyst density equal to

$2.47 \cdot 10^6 \text{ g m}^{-3}$ . The average pore diameter  $d_p$  is established at 1.5 mm. The boundary conditions applied for the reference case are corresponding to the conditions set for the optimization procedure (Section 3.3).

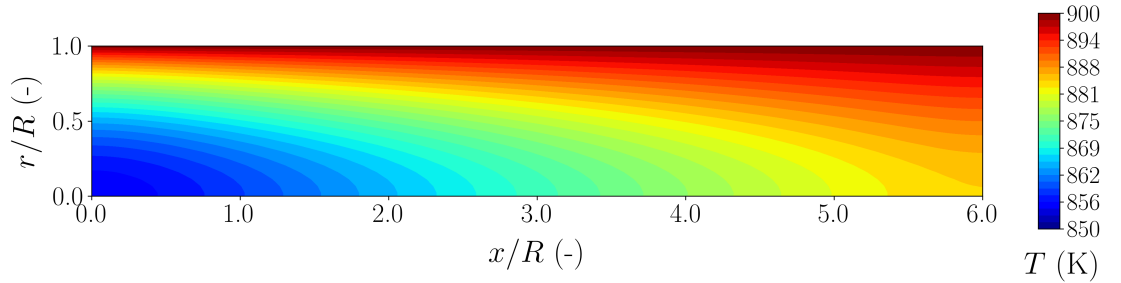


Figure 8: Temperature field distribution - reference case ( $T_{\text{in}} = 900 \text{ K}$ ,  $u_{\text{in}} = 0.15 \text{ m s}^{-1}$ ,  $SC = 2.0$ ,  $\dot{w}_{\text{cat}} = 2.47 \cdot 10^6$ )

The thermal characteristics of the reforming reaction in a conventional reactor can be observed in Fig. 8). The reactor dimensions are divided by the reactor's radius (5 mm), to acquire a dimensionless set of coordinates. Observable temperature gradients are present throughout the whole volume of the reactor. The most significant temperature drop can be noticed at the inlet of the reactor, due to a considerable amount of energy required for the activation of the reforming reaction [41, 37]. The molar fractions of specimens taking part in the process are illustrated in Fig. 9. The molar fractions are averaged over the reactor's radius. Thus, the graph describes the change of the radius-averaged molar fractions in the longitudinal direction of the reactor. The values of the reactor's length are divided by the reactor's radius, to acquire dimensionless values.

The final stage of the numerical analysis predicted the extension of the macro-patterning concept by division of the catalytic insert in the radial direction, forming coaxial segments. The radial segments may accommodate one of two possible configurations. The first variant predicts cylinders with equal width of the inlet surface (Catalyst insert division strategy I), while the second introduces cylinders with an equal area of the inlet surfaces (Catalyst insert division strategy II) (Fig. 1). To allow a direct comparison between each of the composed algorithms, hydrogen productivity  $\zeta$  is introduced.

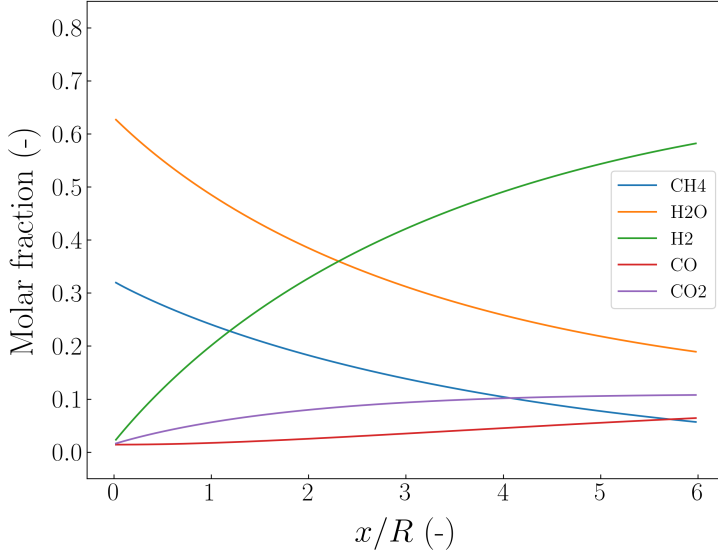


Figure 9: Radius-averaged molar fractions - reference case ( $T_{\text{in}} = 900$  K,  $u_{\text{in}} = 0.15$  m s $^{-1}$ ,  $SC = 2.0$ ,  $\dot{w}_{\text{cat}} = 2.47 \cdot 10^6$ )

Hydrogen productivity delivers insight into the increase of the effectiveness of the reforming reaction for each of the optimized specimens. The  $\zeta$  parameter is an exact ratio of the hydrogen output and the amount of the applied catalyst  $\iota$  for a specific reactor (Eq. (37)). The amount of the catalyst  $\iota$  is calculated as the ratio of the catalyst used in a specific reactor, to the amount of the catalyst applied for the reference case.

$$\zeta = \frac{\text{H}_{2\text{out}}}{\iota} \quad (37)$$

To deliver a comprehensive analysis of specific catalytic insert division strategies, a sensitivity analysis for each of them is conducted. The sensitivity analysis regards changing the weights  $w_{\text{CH}_4}$  and  $w_T$  applied for specific fitness functions (Section ??).

*Thermal fitness 80 %, methane conversion 20 %.*

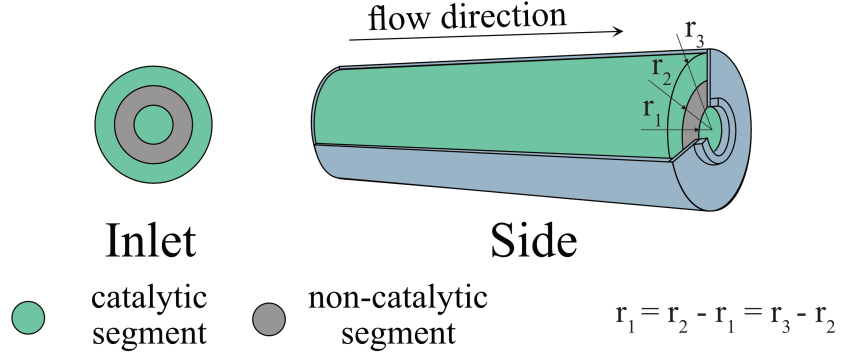


Figure 10: Catalytic insert division strategy I

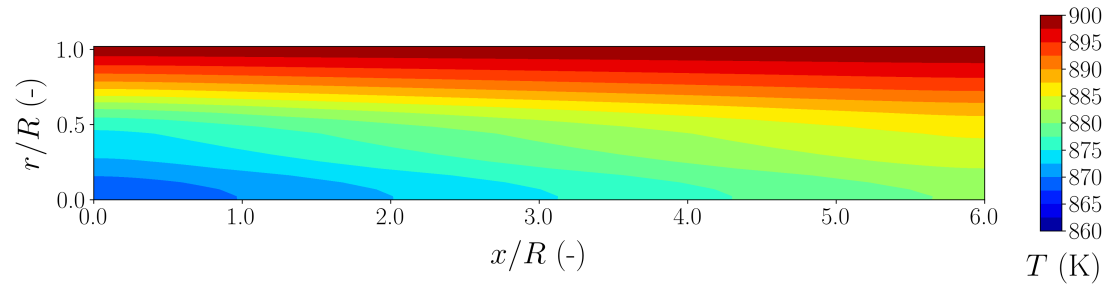


Figure 11: Strategy I - Temperature field distribution - 1<sup>st</sup> generation ( $w_{\text{CH}_4} = 0.2, w_T = 0.8, T_{\text{in}} = 900 \text{ K}, u_{\text{in}} = 0.15 \text{ m s}^{-1}, SC = 2.0$ )

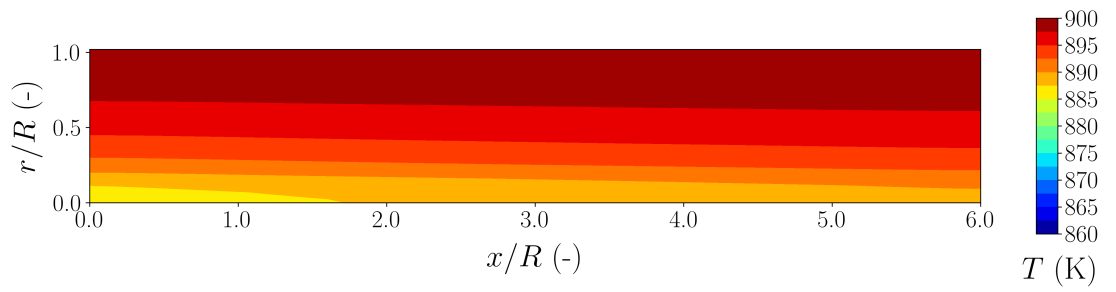


Figure 12: Strategy I - Temperature field distribution - 15<sup>th</sup> generation ( $w_{\text{CH}_4} = 0.2, w_T = 0.8, T_{\text{in}} = 900 \text{ K}, u_{\text{in}} = 0.15 \text{ m s}^{-1}, SC = 2.0$ )

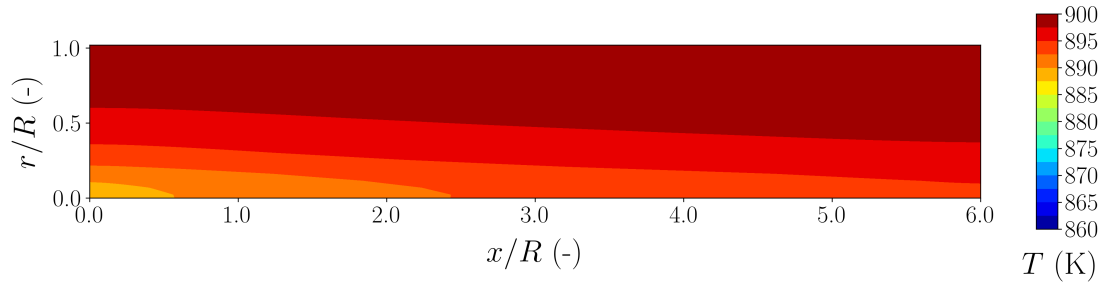


Figure 13: Strategy I - Temperature field distribution - 30<sup>th</sup> generation ( $w_{\text{CH}_4} = 0.2, w_T = 0.8, T_{\text{in}} = 900 \text{ K}, u_{\text{in}} = 0.15 \text{ m s}^{-1}, SC = 2.0$ )

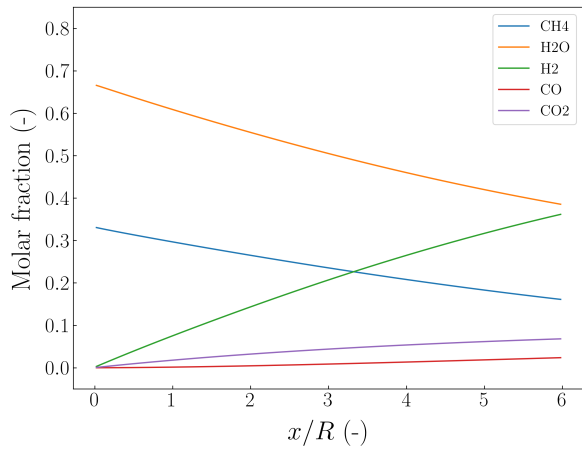


Figure 14: Strategy I - Radius-averaged molar fractions - 1<sup>st</sup> generation ( $w_{\text{CH}_4} = 0.2, w_T = 0.8, T_{\text{in}} = 900 \text{ K}, u_{\text{in}} = 0.15 \text{ m s}^{-1}, SC = 2.0$ )

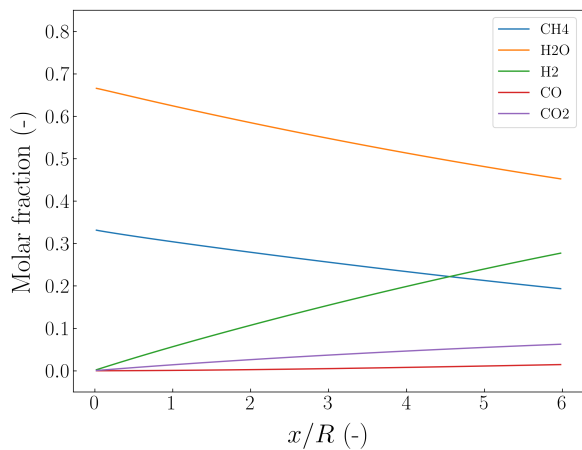


Figure 15: Strategy I - Radius-averaged molar fractions - 15<sup>th</sup> generation ( $w_{\text{CH}_4} = 0.2, w_T = 0.8, T_{\text{in}} = 900 \text{ K}, u_{\text{in}} = 0.15 \text{ m s}^{-1}, SC = 2.0$ )

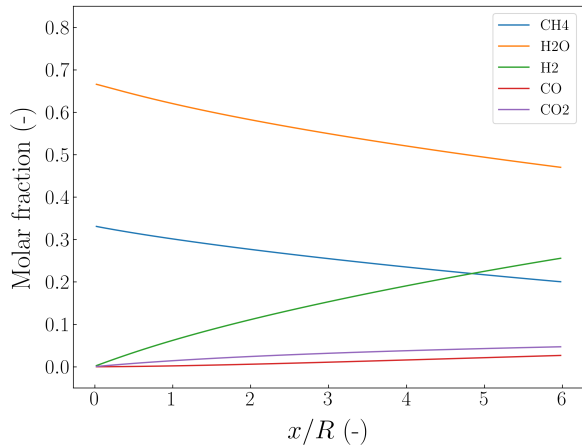


Figure 16: Strategy I - Radius-averaged molar fractions - 30<sup>th</sup> generation ( $w_{\text{CH}_4} = 0.2, w_T = 0.8, T_{\text{in}} = 900 \text{ K}, u_{\text{in}} = 0.15 \text{ m s}^{-1}, SC = 2.0$ )

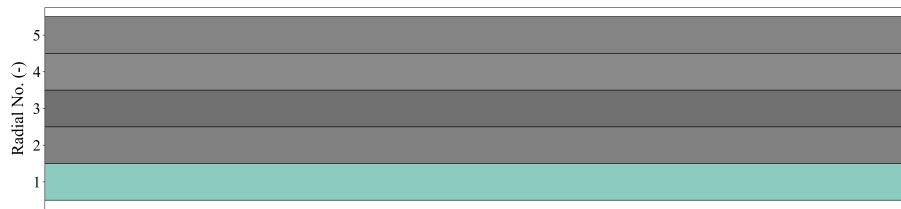


Figure 17: Strategy I - Segments distribution for 30<sup>th</sup> generation ( $w_{\text{CH}_4} = 0.2, w_T = 0.8, T_{\text{in}} = 900 \text{ K}, u_{\text{in}} = 0.15 \text{ m s}^{-1}, SC = 2.0$ )

*Thermal fitness 60 %, methane conversion 40 %.*

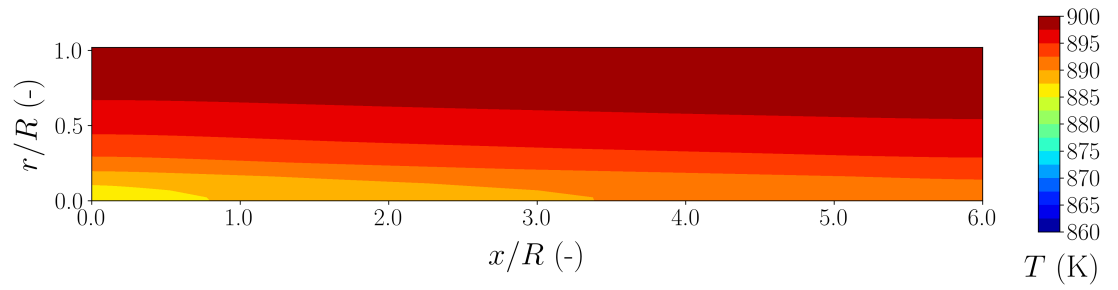


Figure 18: Strategy I - Temperature field distribution - 1<sup>st</sup> generation ( $w_{\text{CH}_4} = 0.4, w_T = 0.6, T_{\text{in}} = 900 \text{ K}, u_{\text{in}} = 0.15 \text{ m s}^{-1}, SC = 2.0$ )

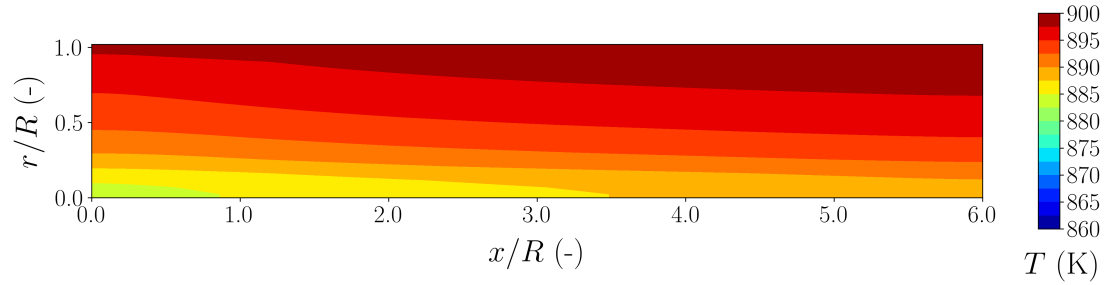


Figure 19: Strategy I - Temperature field distribution - 15<sup>th</sup> generation ( $w_{\text{CH}_4} = 0.4, w_T = 0.6, T_{\text{in}} = 900 \text{ K}, u_{\text{in}} = 0.15 \text{ m s}^{-1}, SC = 2.0$ )

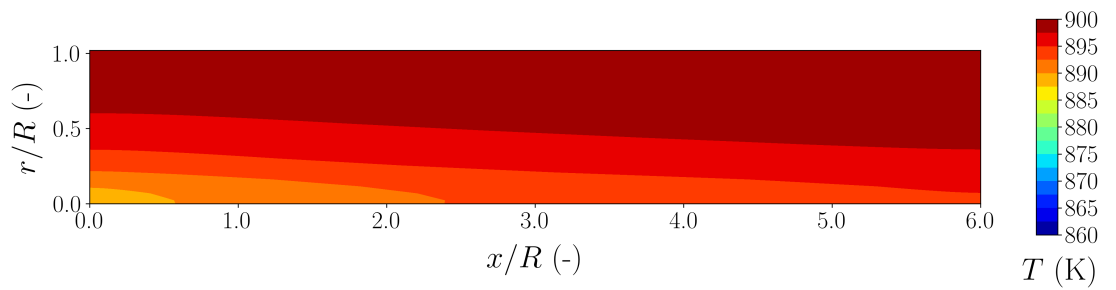


Figure 20: Strategy I - Temperature field distribution - 30<sup>th</sup> generation ( $w_{\text{CH}_4} = 0.4, w_T = 0.6, T_{\text{in}} = 900 \text{ K}, u_{\text{in}} = 0.15 \text{ m s}^{-1}, SC = 2.0$ )

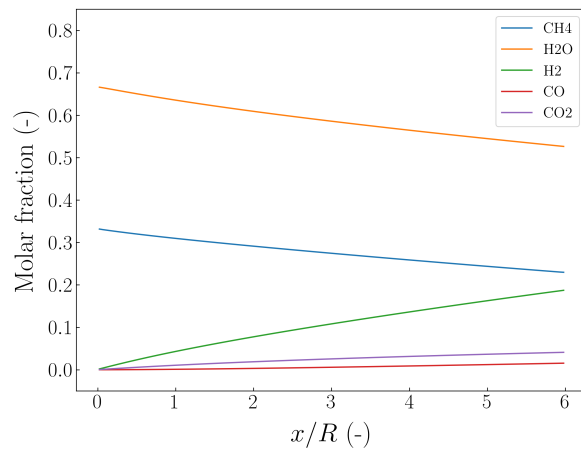


Figure 21: Strategy I - Radius-averaged molar fractions - 1<sup>st</sup> generation ( $w_{\text{CH}_4} = 0.4, w_T = 0.6, T_{\text{in}} = 900 \text{ K}, u_{\text{in}} = 0.15 \text{ m s}^{-1}, SC = 2.0$ )

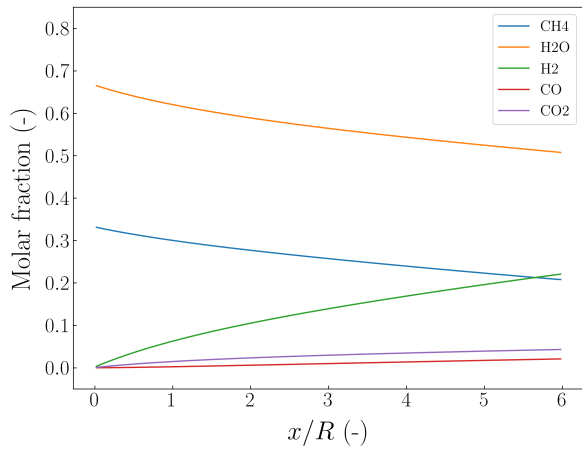


Figure 22: Strategy I - Radius-averaged molar fractions - 15<sup>th</sup> generation ( $w_{\text{CH}_4} = 0.4, w_T = 0.6, T_{\text{in}} = 900 \text{ K}, u_{\text{in}} = 0.15 \text{ m s}^{-1}, SC = 2.0$ )

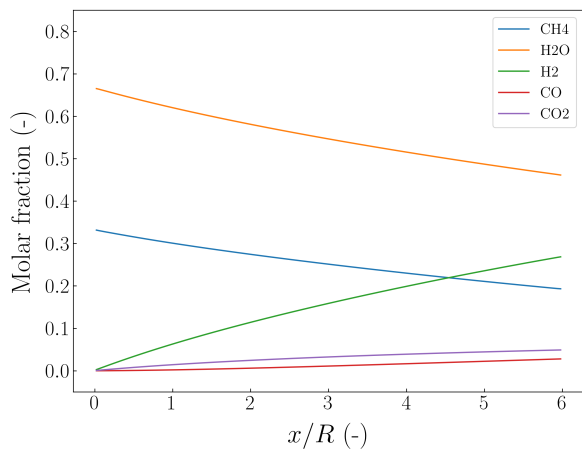


Figure 23: Strategy I - Radius-averaged molar fractions - 30<sup>th</sup> generation ( $w_{\text{CH}_4} = 0.4, w_T = 0.6, T_{\text{in}} = 900 \text{ K}, u_{\text{in}} = 0.15 \text{ m s}^{-1}, SC = 2.0$ )

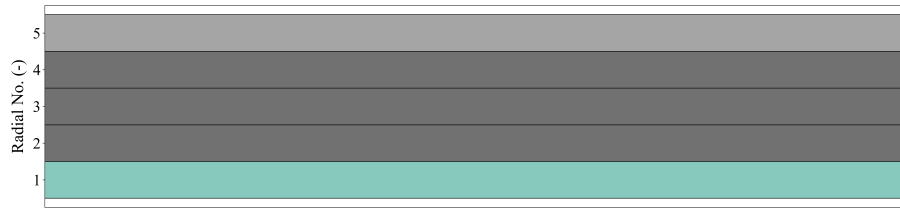


Figure 24: Strategy I - Segments distribution for 30<sup>th</sup> generation ( $w_{\text{CH}_4} = 0.4, w_T = 0.6, T_{\text{in}} = 900 \text{ K}, u_{\text{in}} = 0.15 \text{ m s}^{-1}, SC = 2.0$ )

*Thermal fitness 50 %, methane conversion 50 %.*

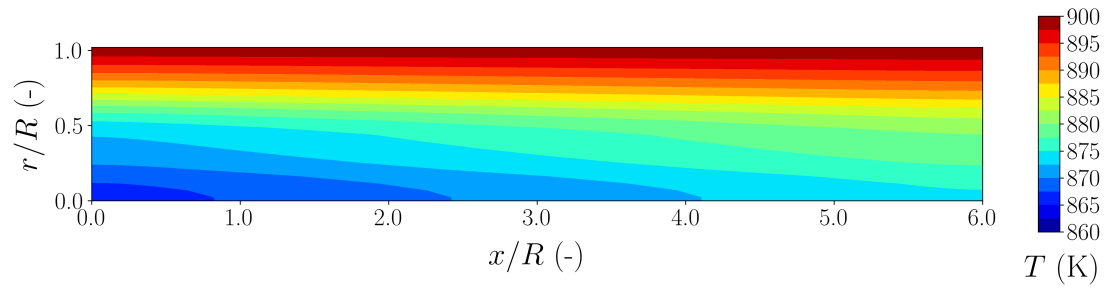


Figure 25: Strategy I - Temperature field distribution - 1<sup>st</sup> generation ( $w_{\text{CH}_4} = 0.5, w_T = 0.5, T_{\text{in}} = 900 \text{ K}, u_{\text{in}} = 0.15 \text{ m s}^{-1}, SC = 2.0$ )

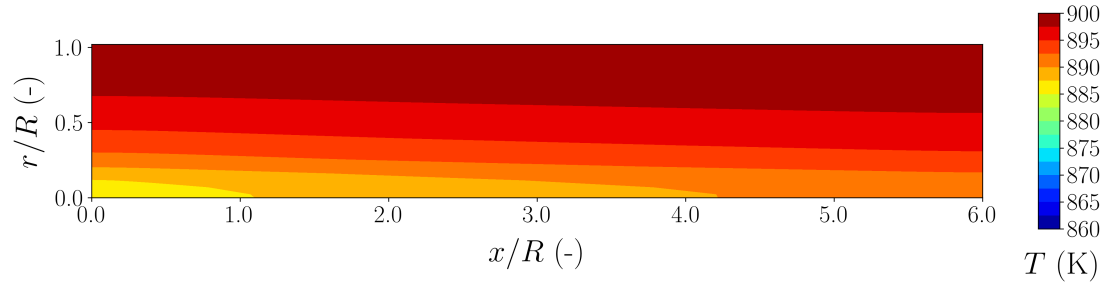


Figure 26: Strategy I - Temperature field distribution - 15<sup>th</sup> generation ( $w_{\text{CH}_4} = 0.5, w_T = 0.5, T_{\text{in}} = 900 \text{ K}, u_{\text{in}} = 0.15 \text{ m s}^{-1}, SC = 2.0$ )

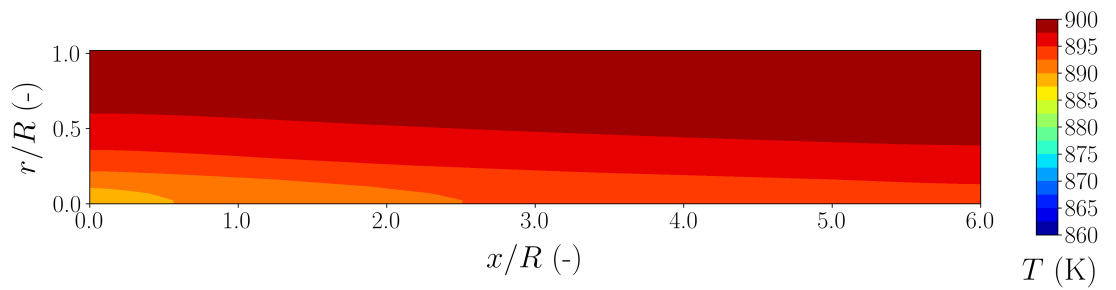


Figure 27: Strategy I - Temperature field distribution - 30<sup>th</sup> generation ( $w_{\text{CH}_4} = 0.5, w_T = 0.5, T_{\text{in}} = 900 \text{ K}, u_{\text{in}} = 0.15 \text{ m s}^{-1}, SC = 2.0$ )

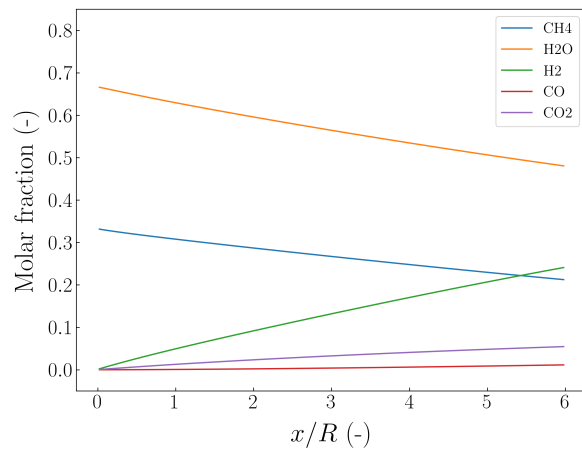


Figure 28: Strategy I - Radius-averaged molar fractions - 1<sup>st</sup> generation ( $w_{\text{CH}_4} = 0.5, w_T = 0.5, T_{\text{in}} = 900 \text{ K}, u_{\text{in}} = 0.15 \text{ m s}^{-1}, SC = 2.0$ )

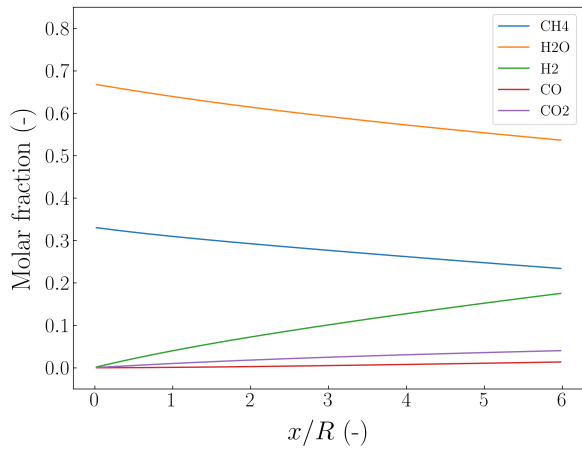


Figure 29: Strategy I - Radius-averaged molar fractions - 15<sup>th</sup> generation ( $w_{\text{CH}_4} = 0.5, w_T = 0.5, T_{\text{in}} = 900 \text{ K}, u_{\text{in}} = 0.15 \text{ m s}^{-1}, SC = 2.0$ )

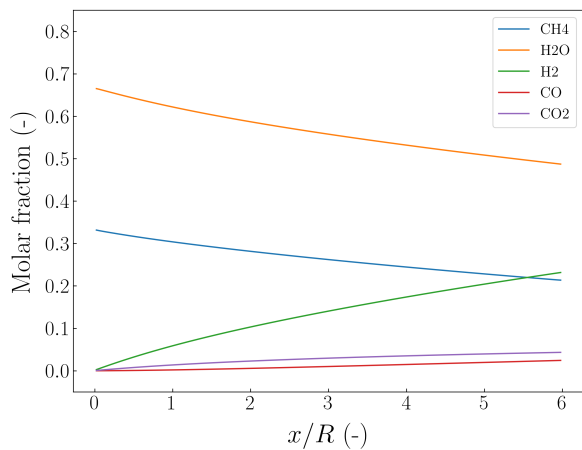


Figure 30: Strategy I - Radius-averaged molar fractions - 30<sup>th</sup> generation ( $w_{\text{CH}_4} = 0.5, w_T = 0.5, T_{\text{in}} = 900 \text{ K}, u_{\text{in}} = 0.15 \text{ m s}^{-1}, SC = 2.0$ )

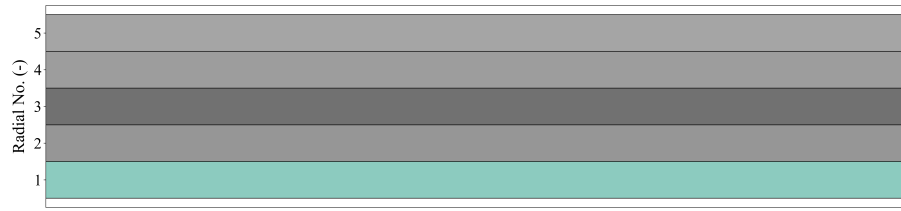


Figure 31: Strategy I - Segments distribution for 30<sup>th</sup> generation ( $w_{\text{CH}_4} = 0.5, w_T = 0.5, T_{\text{in}} = 900 \text{ K}, u_{\text{in}} = 0.15 \text{ m s}^{-1}, SC = 2.0$ )

*Thermal fitness 40 %, methane conversion 60 %.*

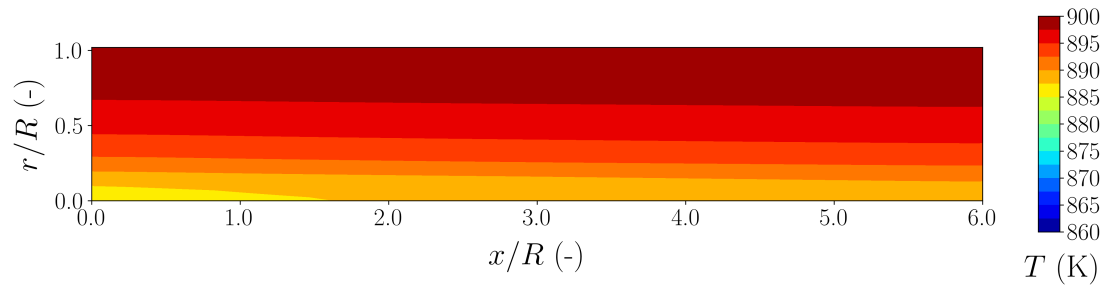


Figure 32: Strategy I - Temperature field distribution - 1<sup>st</sup> generation ( $w_{\text{CH}_4} = 0.6, w_T = 0.4, T_{\text{in}} = 900 \text{ K}, u_{\text{in}} = 0.15 \text{ m s}^{-1}, SC = 2.0$ )

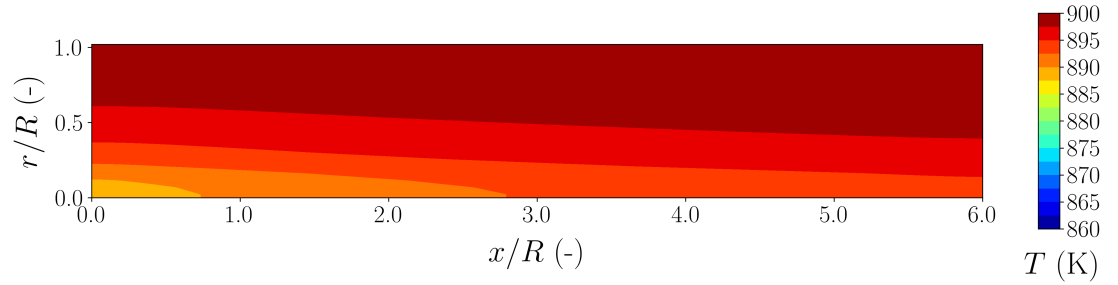


Figure 33: Strategy I - Temperature field distribution - 15<sup>th</sup> generation ( $w_{\text{CH}_4} = 0.6, w_T = 0.4, T_{\text{in}} = 900 \text{ K}, u_{\text{in}} = 0.15 \text{ m s}^{-1}, SC = 2.0$ )

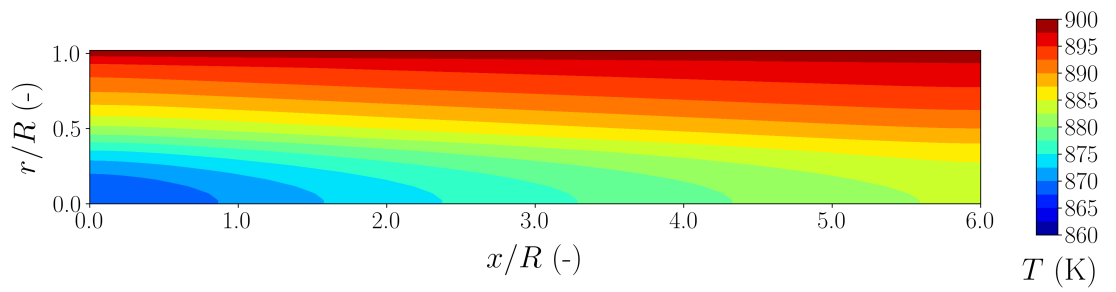


Figure 34: Strategy I - Temperature field distribution - 30<sup>th</sup> generation ( $w_{\text{CH}_4} = 0.6, w_T = 0.4, T_{\text{in}} = 900 \text{ K}, u_{\text{in}} = 0.15 \text{ m s}^{-1}, SC = 2.0$ )

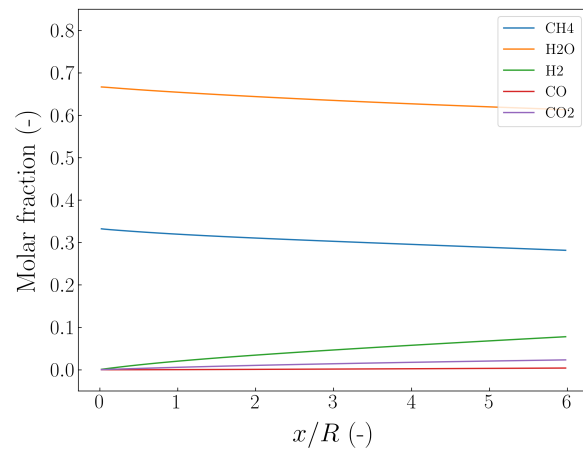


Figure 35: Strategy I - Radius-averaged molar fractions - 1<sup>st</sup> generation ( $w_{\text{CH}_4} = 0.6, w_T = 0.4, T_{\text{in}} = 900 \text{ K}, u_{\text{in}} = 0.15 \text{ m s}^{-1}, SC = 2.0$ )

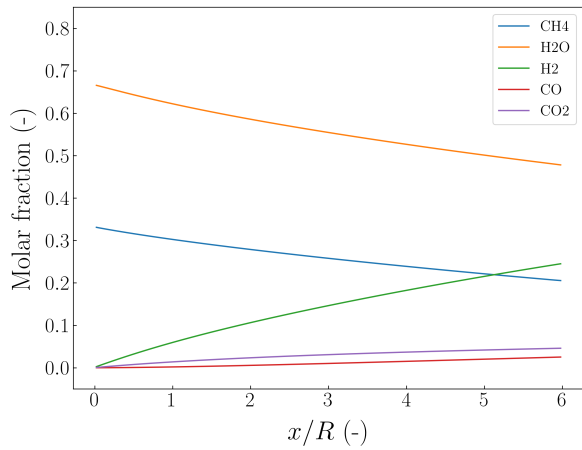


Figure 36: Strategy I - Radius-averaged molar fractions - 15<sup>th</sup> generation ( $w_{\text{CH}_4} = 0.6, w_T = 0.4, T_{\text{in}} = 900 \text{ K}, u_{\text{in}} = 0.15 \text{ m s}^{-1}, SC = 2.0$ )

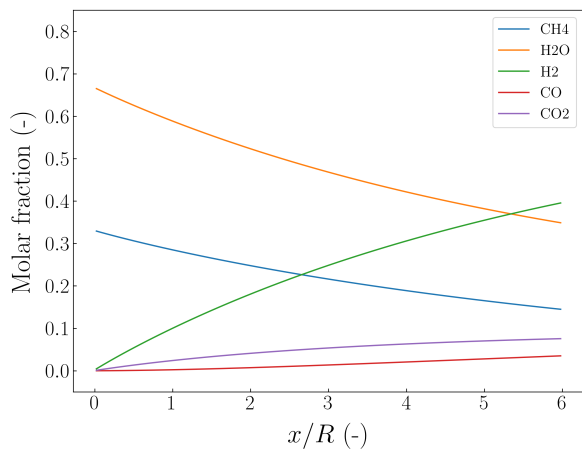


Figure 37: Strategy I - Radius-averaged molar fractions - 30<sup>th</sup> generation ( $w_{\text{CH}_4} = 0.6, w_T = 0.4, T_{\text{in}} = 900 \text{ K}, u_{\text{in}} = 0.15 \text{ m s}^{-1}, SC = 2.0$ )



Figure 38: Strategy I - Segments distribution for 30<sup>th</sup> generation ( $w_{\text{CH}_4} = 0.6, w_T = 0.4, T_{\text{in}} = 900 \text{ K}, u_{\text{in}} = 0.15 \text{ m s}^{-1}, SC = 2.0$ )

*Thermal fitness 20 %, methane conversion 80 %.*

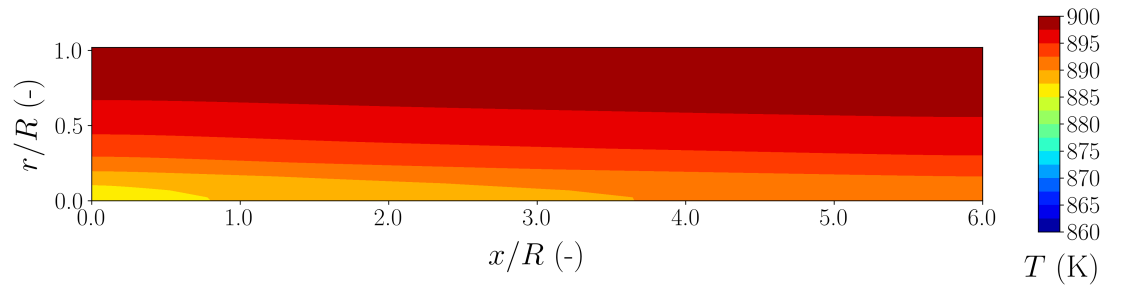


Figure 39: Strategy I - Temperature field distribution - 1<sup>st</sup> generation ( $w_{\text{CH}_4} = 0.8, w_T = 0.2, T_{\text{in}} = 900 \text{ K}, u_{\text{in}} = 0.15 \text{ m s}^{-1}, SC = 2.0$ )

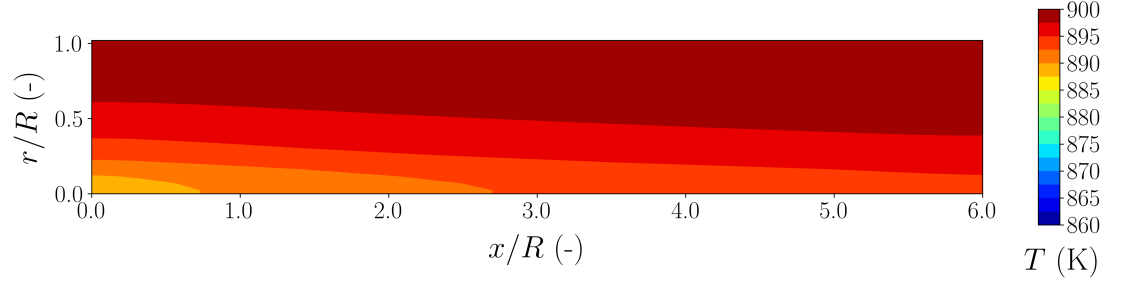


Figure 40: Strategy I - Temperature field distribution - 15<sup>th</sup> generation ( $w_{\text{CH}_4} = 0.8, w_T = 0.2, T_{\text{in}} = 900 \text{ K}, u_{\text{in}} = 0.15 \text{ m s}^{-1}, SC = 2.0$ )

The development of the fitness values among successive populations for strategy I is presented in Fig. ??.

To allow a straightforward comparison between the catalyst inserts division strategies, hydrogen productivity  $\zeta$  is calculated for the optimal cases found by each algorithm. The hydrogen productivity is summarized in Table 5.

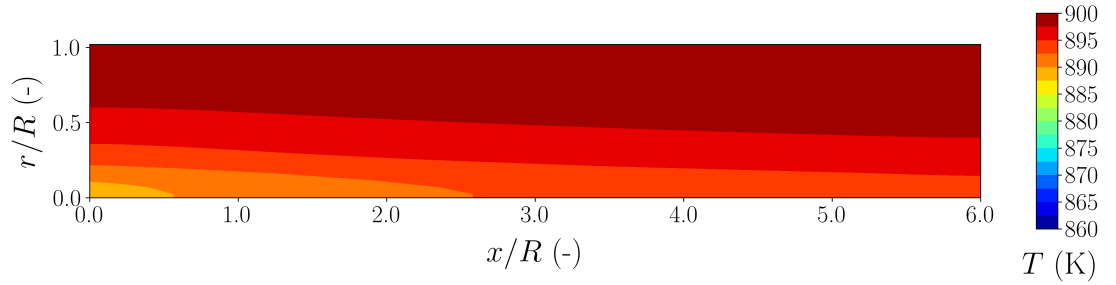


Figure 41: Strategy I - Temperature field distribution - 30<sup>th</sup> generation ( $w_{\text{CH}_4} = 0.8, w_T = 0.2, T_{\text{in}} = 900 \text{ K}, u_{\text{in}} = 0.15 \text{ m s}^{-1}, SC = 2.0$ )

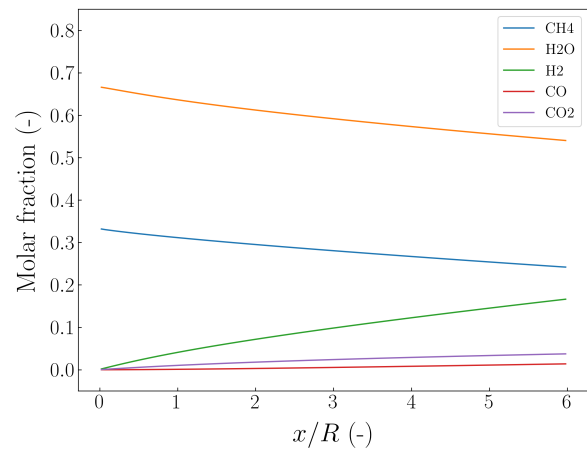


Figure 42: Strategy I - Radius-averaged molar fractions - 1<sup>st</sup> generation ( $w_{\text{CH}_4} = 0.8, w_T = 0.2, T_{\text{in}} = 900 \text{ K}, u_{\text{in}} = 0.15 \text{ m s}^{-1}, SC = 2.0$ )

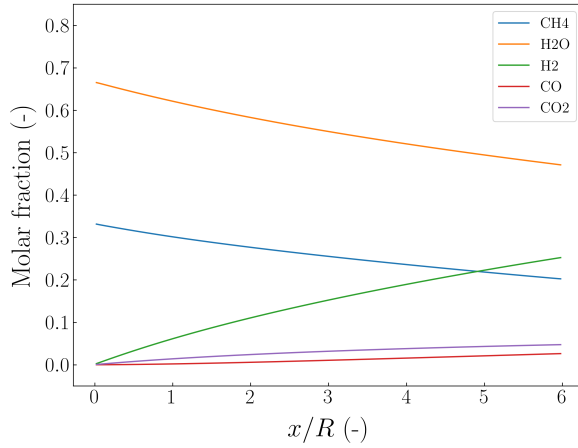


Figure 43: Strategy I - Radius-averaged molar fractions - 15<sup>th</sup> generation ( $w_{\text{CH}_4} = 0.8, w_T = 0.2, T_{\text{in}} = 900 \text{ K}, u_{\text{in}} = 0.15 \text{ m s}^{-1}, SC = 2.0$ )

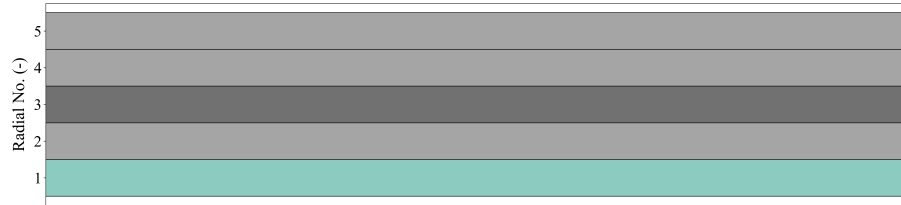


Figure 44: Strategy I - Segments distribution for 30<sup>th</sup> generation ( $w_{\text{CH}_4} = 0.8, w_T = 0.2, T_{\text{in}} = 900 \text{ K}, u_{\text{in}} = 0.15 \text{ m s}^{-1}, SC = 2.0$ )

Table 4: Hydrogen productivity for the catalytic insert division strategy I

$w_{\text{CH}_4} / w_T$	$\text{H}_{2\text{out}}$	$\iota$	$\zeta$
REF	0.581	1.00	0.581
0.2 / 0.8	0.255	0.20	1.278
0.4 / 0.6	0.268	0.19	1.398
0.5 / 0.5	0.231	0.20	1.157
0.6 / 0.4	0.407	0.45	0.900
0.8 / 0.2	0.218	0.20	1.090

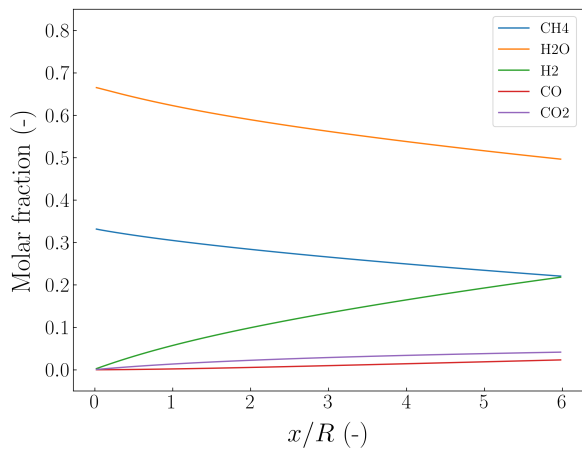


Figure 45: Strategy I - Radius-averaged molar fractions - 30<sup>th</sup> generation ( $w_{\text{CH}_4} = 0.8, w_T = 0.2, T_{\text{in}} = 900 \text{ K}, u_{\text{in}} = 0.15 \text{ m s}^{-1}, SC = 2.0$ )

### 5.1. Insert division strategy II

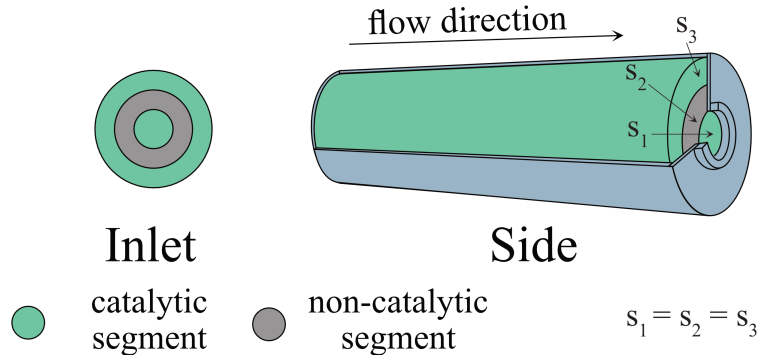


Figure 46: Catalytic insert division strategy II

*Thermal fitness 80 %, methane conversion 20 %.*

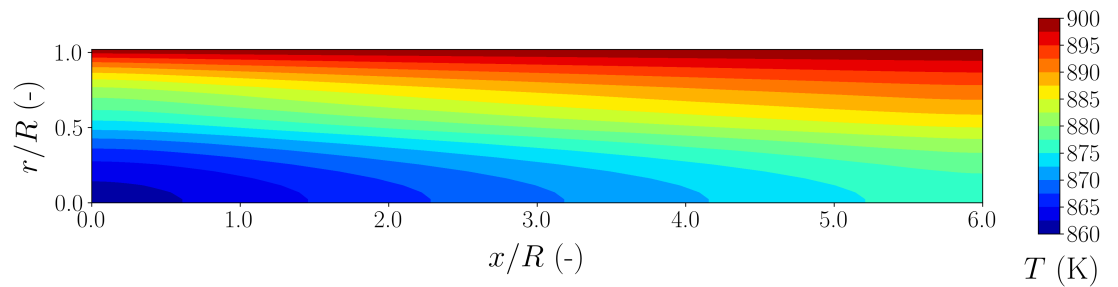


Figure 47: Strategy II - Temperature field distribution - 1<sup>st</sup> generation ( $w_{\text{CH}_4} = 0.2, w_T = 0.8, T_{\text{in}} = 900 \text{ K}, u_{\text{in}} = 0.15 \text{ m s}^{-1}, SC = 2.0$ )

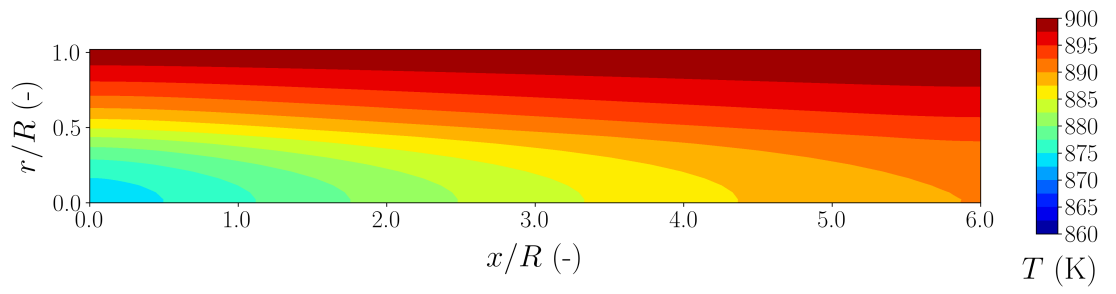


Figure 48: Strategy II - Temperature field distribution - 15<sup>th</sup> generation ( $w_{\text{CH}_4} = 0.2, w_T = 0.8, T_{\text{in}} = 900 \text{ K}, u_{\text{in}} = 0.15 \text{ m s}^{-1}, SC = 2.0$ )

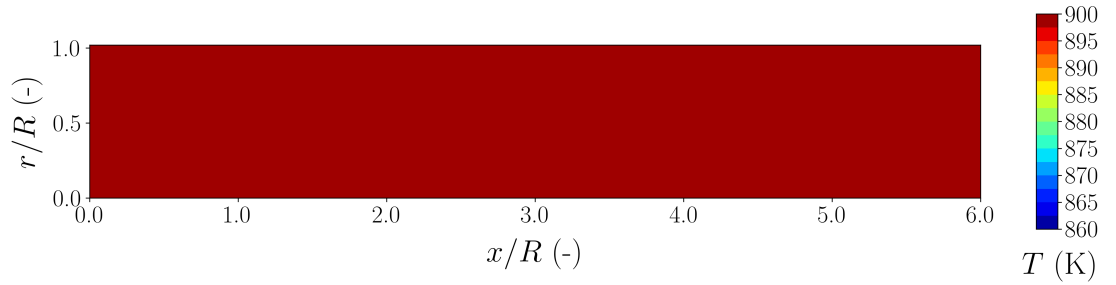


Figure 49: Strategy II - Temperature field distribution - 30<sup>th</sup> generation ( $w_{\text{CH}_4} = 0.2, w_T = 0.8, T_{\text{in}} = 900 \text{ K}, u_{\text{in}} = 0.15 \text{ m s}^{-1}, SC = 2.0$ )

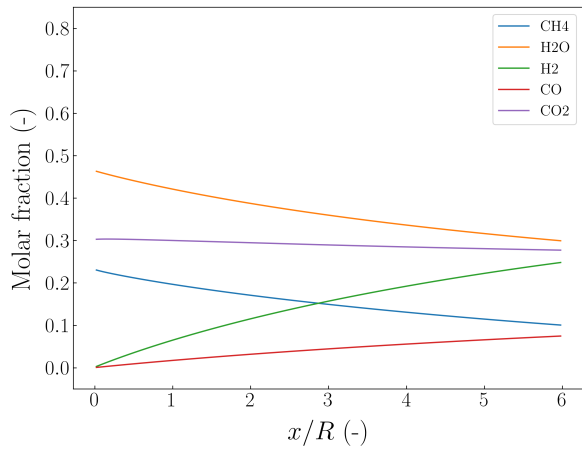


Figure 50: Strategy II - Radius-averaged molar fractions - 1<sup>st</sup> generation ( $w_{\text{CH}_4} = 0.2, w_T = 0.8, T_{\text{in}} = 900 \text{ K}, u_{\text{in}} = 0.15 \text{ m s}^{-1}, SC = 2.0$ )

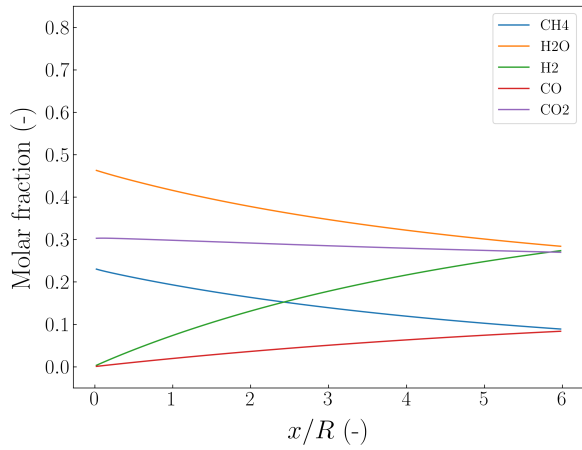


Figure 51: Strategy II - Radius-averaged molar fractions - 15<sup>th</sup> generation ( $w_{\text{CH}_4} = 0.2, w_T = 0.8, T_{\text{in}} = 900 \text{ K}, u_{\text{in}} = 0.15 \text{ m s}^{-1}, SC = 2.0$ )

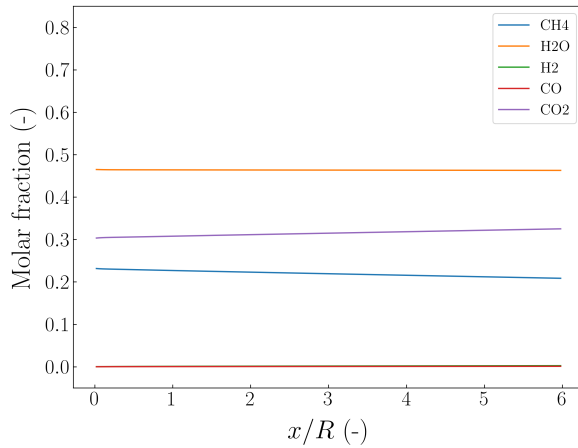


Figure 52: Strategy II - Radius-averaged molar fractions - 30<sup>th</sup> generation ( $w_{\text{CH}_4} = 0.2, w_T = 0.8, T_{\text{in}} = 900 \text{ K}, u_{\text{in}} = 0.15 \text{ m s}^{-1}, SC = 2.0$ )

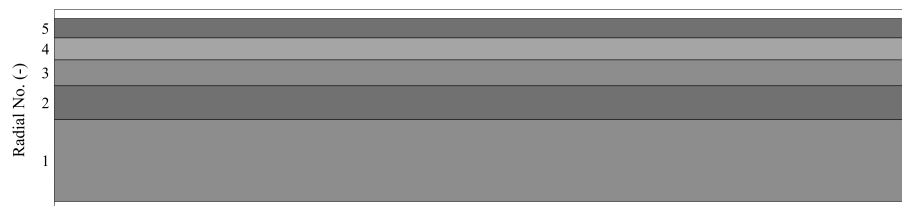


Figure 53: Strategy II - Segments distribution for 30<sup>th</sup> generation ( $w_{\text{CH}_4} = 0.2, w_T = 0.8, T_{\text{in}} = 900 \text{ K}, u_{\text{in}} = 0.15 \text{ m s}^{-1}, SC = 2.0$ )

*Thermal fitness 60 %, methane conversion 40 %.*

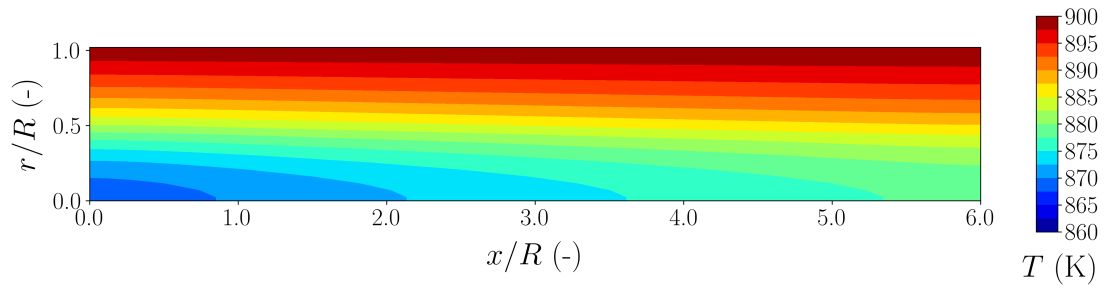


Figure 54: Strategy II - Temperature field distribution - 1<sup>st</sup> generation ( $w_{\text{CH}_4} = 0.4, w_T = 0.6, T_{\text{in}} = 900 \text{ K}, u_{\text{in}} = 0.15 \text{ m s}^{-1}, SC = 2.0$ )

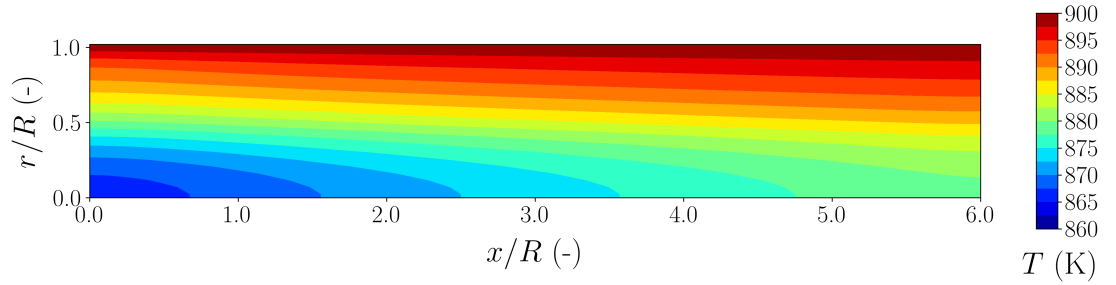


Figure 55: Strategy II - Temperature field distribution - 15<sup>th</sup> generation ( $w_{\text{CH}_4} = 0.4, w_T = 0.6, T_{\text{in}} = 900 \text{ K}, u_{\text{in}} = 0.15 \text{ m s}^{-1}, SC = 2.0$ )

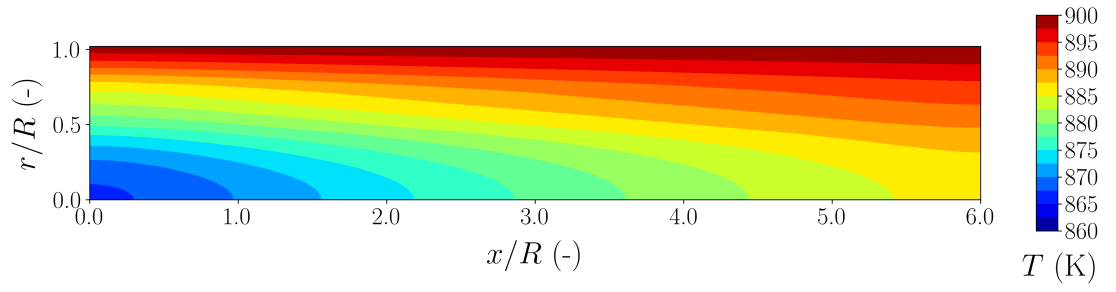


Figure 56: Strategy II - Temperature field distribution - 30<sup>th</sup> generation ( $w_{\text{CH}_4} = 0.4, w_T = 0.6, T_{\text{in}} = 900 \text{ K}, u_{\text{in}} = 0.15 \text{ m s}^{-1}, SC = 2.0$ )

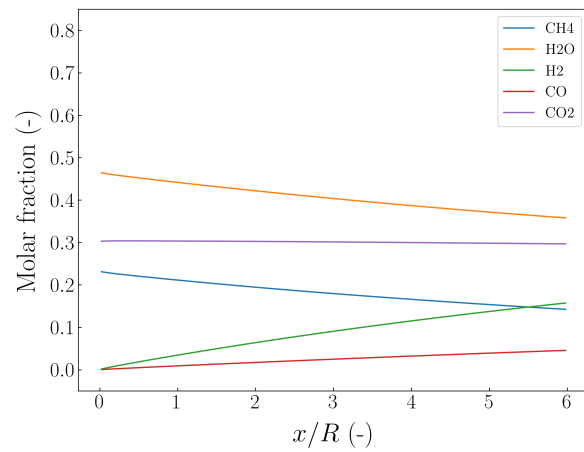


Figure 57: Strategy II - Radius-averaged molar fractions - 1<sup>st</sup> generation ( $w_{\text{CH}_4} = 0.4, w_T = 0.6, T_{\text{in}} = 900 \text{ K}, u_{\text{in}} = 0.15 \text{ m s}^{-1}, SC = 2.0$ )

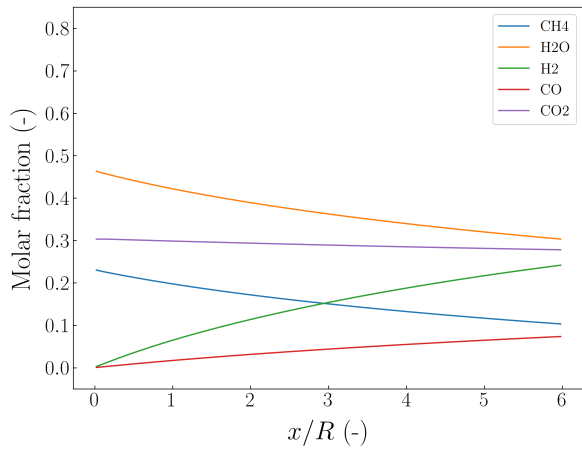


Figure 58: Strategy II - Radius-averaged molar fractions - 15<sup>th</sup> generation ( $w_{\text{CH}_4} = 0.4, w_T = 0.6, T_{\text{in}} = 900 \text{ K}, u_{\text{in}} = 0.15 \text{ m s}^{-1}, SC = 2.0$ )

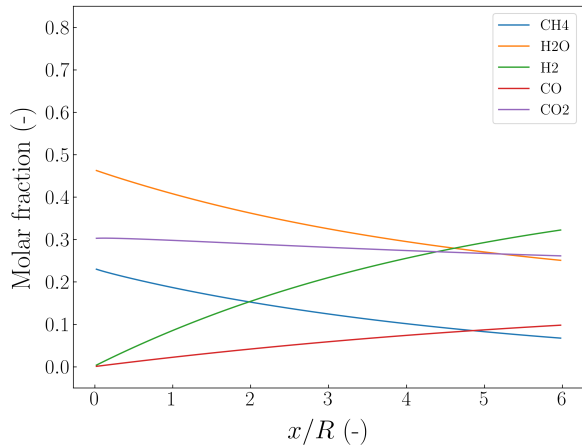


Figure 59: Strategy II - Radius-averaged molar fractions - 30<sup>th</sup> generation ( $w_{\text{CH}_4} = 0.4, w_T = 0.6, T_{\text{in}} = 900 \text{ K}, u_{\text{in}} = 0.15 \text{ m s}^{-1}, SC = 2.0$ )

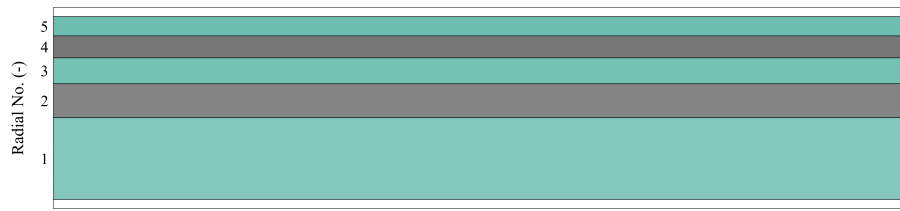


Figure 60: Strategy II - Segments distribution for 30<sup>th</sup> generation ( $w_{\text{CH}_4} = 0.4, w_T = 0.6, T_{\text{in}} = 900 \text{ K}, u_{\text{in}} = 0.15 \text{ m s}^{-1}, SC = 2.0$ )

*Thermal fitness 50 %, methane conversion 50 %.*

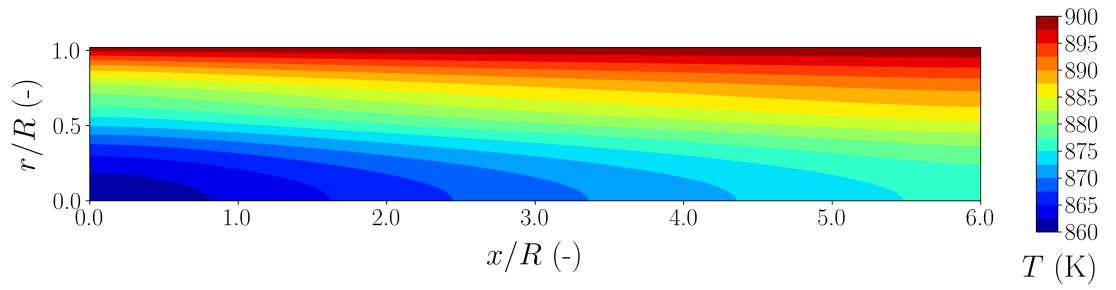


Figure 61: Strategy II - Temperature field distribution - 1<sup>st</sup> generation ( $w_{\text{CH}_4} = 0.5, w_T = 0.5, T_{\text{in}} = 900 \text{ K}, u_{\text{in}} = 0.15 \text{ m s}^{-1}, SC = 2.0$ )

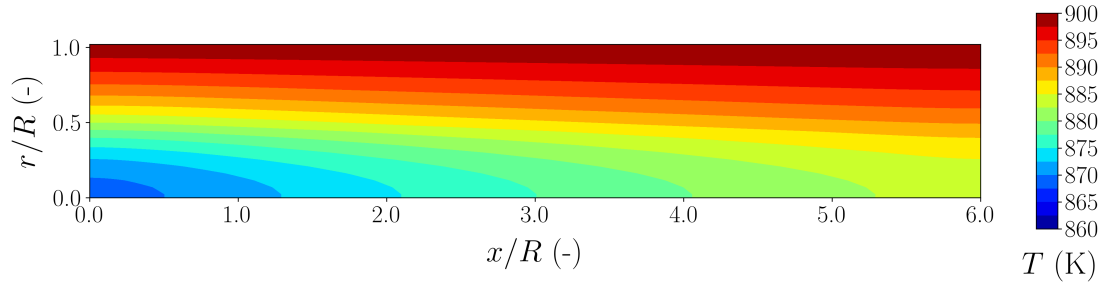


Figure 62: Strategy II - Temperature field distribution - 15<sup>th</sup> generation ( $w_{\text{CH}_4} = 0.5, w_T = 0.5, T_{\text{in}} = 900 \text{ K}, u_{\text{in}} = 0.15 \text{ m s}^{-1}, SC = 2.0$ )

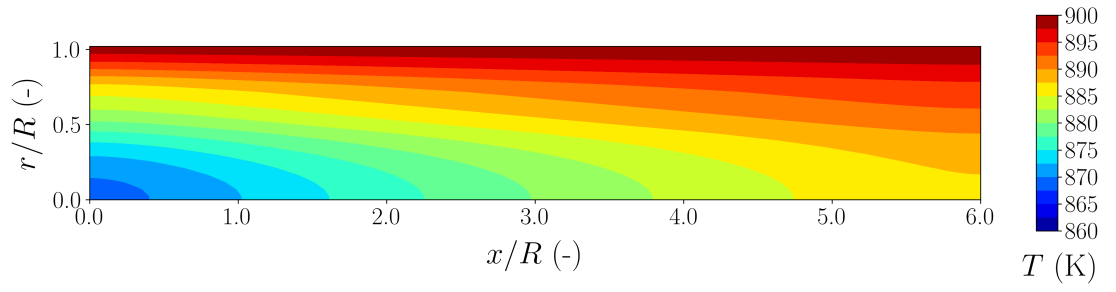


Figure 63: Strategy II - Temperature field distribution - 30<sup>th</sup> generation ( $w_{\text{CH}_4} = 0.5, w_T = 0.5, T_{\text{in}} = 900 \text{ K}, u_{\text{in}} = 0.15 \text{ m s}^{-1}, SC = 2.0$ )

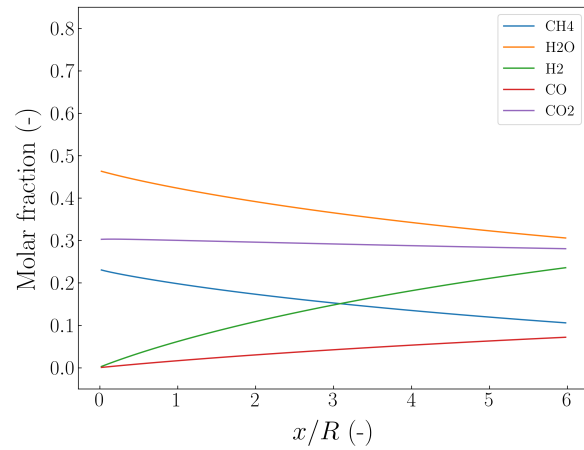


Figure 64: Strategy II - Radius-averaged molar fractions - 1<sup>st</sup> generation ( $w_{\text{CH}_4} = 0.5, w_T = 0.5, T_{\text{in}} = 900 \text{ K}, u_{\text{in}} = 0.15 \text{ m s}^{-1}, SC = 2.0$ )

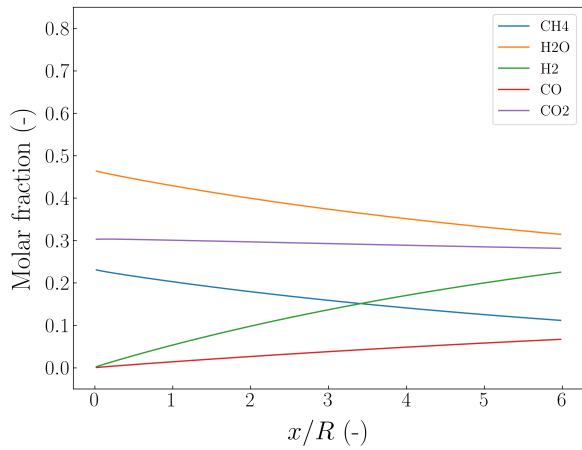


Figure 65: Strategy II - Radius-averaged molar fractions - 15<sup>th</sup> generation ( $w_{\text{CH}_4} = 0.5, w_T = 0.5, T_{\text{in}} = 900 \text{ K}, u_{\text{in}} = 0.15 \text{ m s}^{-1}, SC = 2.0$ )

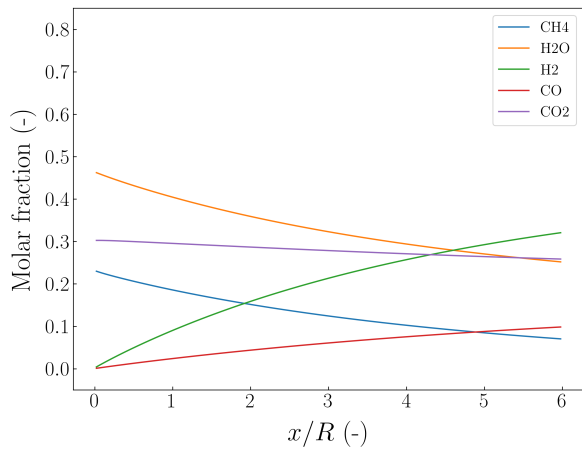


Figure 66: Strategy II - Radius-averaged molar fractions - 30<sup>th</sup> generation ( $w_{\text{CH}_4} = 0.5, w_T = 0.5, T_{\text{in}} = 900 \text{ K}, u_{\text{in}} = 0.15 \text{ m s}^{-1}, SC = 2.0$ )

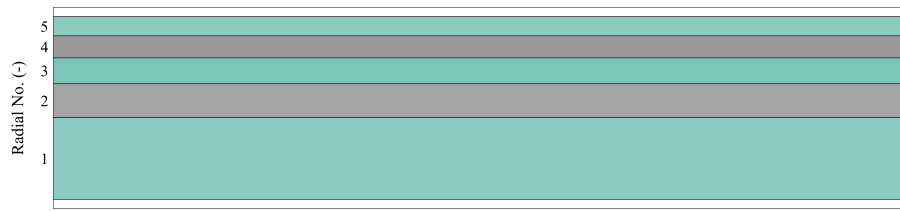


Figure 67: Strategy II - Segments distribution for 30<sup>th</sup> generation ( $w_{\text{CH}_4} = 0.5, w_T = 0.5, T_{\text{in}} = 900 \text{ K}, u_{\text{in}} = 0.15 \text{ m s}^{-1}, SC = 2.0$ )

*Thermal fitness 40 %, methane conversion 60 %.*

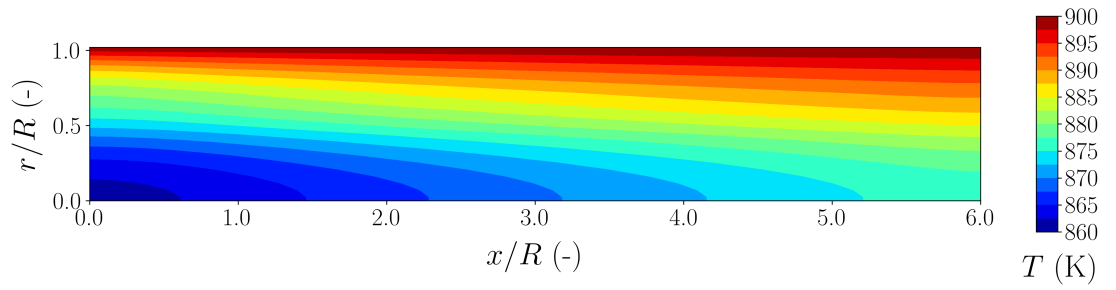


Figure 68: Strategy II - Temperature field distribution - 1<sup>st</sup> generation ( $w_{\text{CH}_4} = 0.6, w_T = 0.4, T_{\text{in}} = 900 \text{ K}, u_{\text{in}} = 0.15 \text{ m s}^{-1}, SC = 2.0$ )

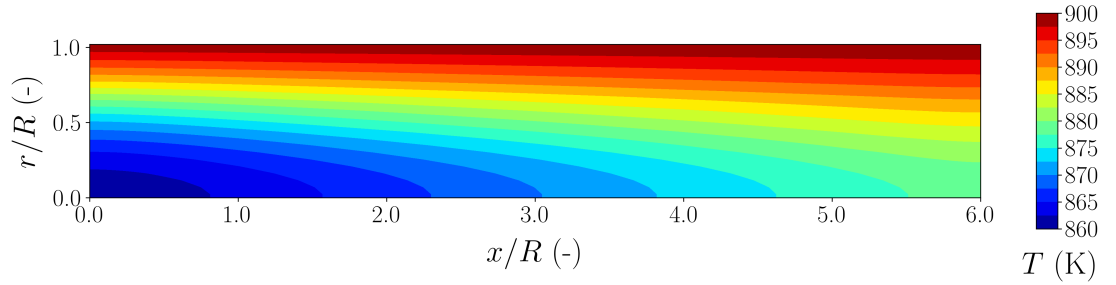


Figure 69: Strategy II - Temperature field distribution - 15<sup>th</sup> generation ( $w_{\text{CH}_4} = 0.6, w_T = 0.4, T_{\text{in}} = 900 \text{ K}, u_{\text{in}} = 0.15 \text{ m s}^{-1}, SC = 2.0$ )

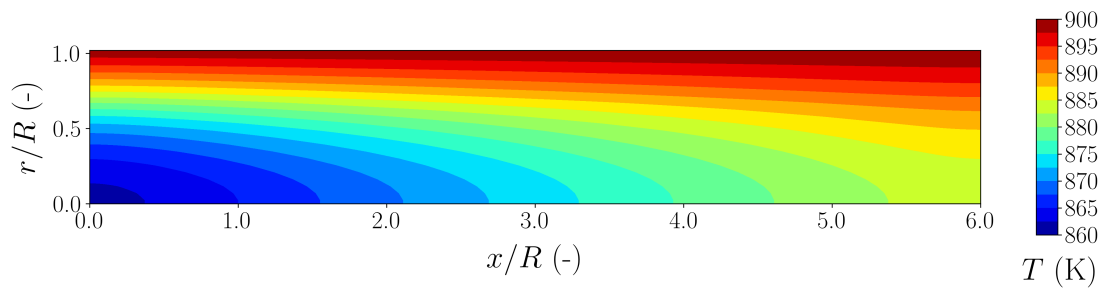


Figure 70: Strategy II - Temperature field distribution - 30<sup>th</sup> generation ( $w_{\text{CH}_4} = 0.6, w_T = 0.4, T_{\text{in}} = 900 \text{ K}, u_{\text{in}} = 0.15 \text{ m s}^{-1}, SC = 2.0$ )

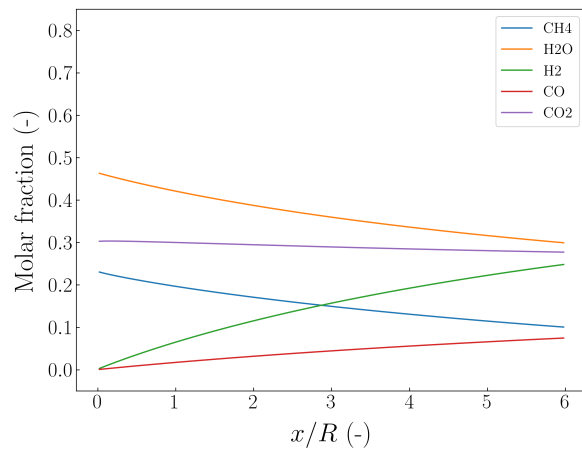


Figure 71: Strategy II - Radius-averaged molar fractions - 1<sup>st</sup> generation ( $w_{\text{CH}_4} = 0.6, w_T = 0.4, T_{\text{in}} = 900 \text{ K}, u_{\text{in}} = 0.15 \text{ m s}^{-1}, SC = 2.0$ )

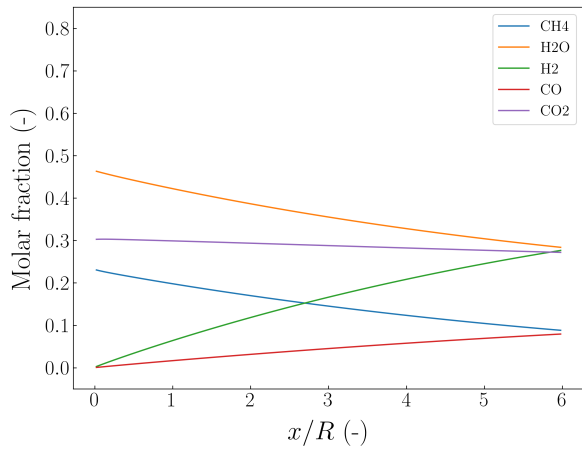


Figure 72: Strategy II - Radius-averaged molar fractions - 15<sup>th</sup> generation ( $w_{\text{CH}_4} = 0.6, w_T = 0.4, T_{\text{in}} = 900 \text{ K}, u_{\text{in}} = 0.15 \text{ m s}^{-1}, SC = 2.0$ )

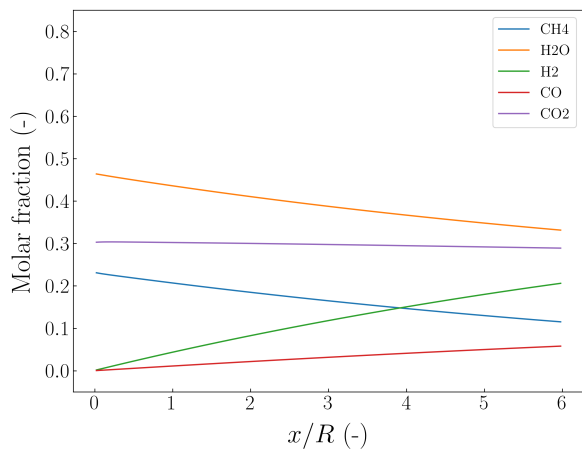


Figure 73: Strategy II - Radius-averaged molar fractions - 30<sup>th</sup> generation ( $w_{\text{CH}_4} = 0.6, w_T = 0.4, T_{\text{in}} = 900 \text{ K}, u_{\text{in}} = 0.15 \text{ m s}^{-1}, SC = 2.0$ )

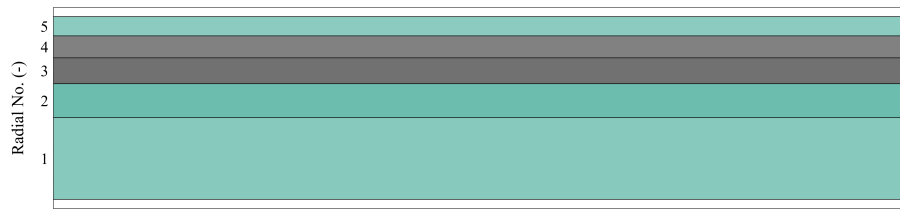


Figure 74: Strategy II - Segments distribution for 30<sup>th</sup> generation ( $w_{\text{CH}_4} = 0.6, w_T = 0.4, T_{\text{in}} = 900 \text{ K}, u_{\text{in}} = 0.15 \text{ m s}^{-1}, SC = 2.0$ )

*Thermal fitness 20 %, methane conversion 80 %.*

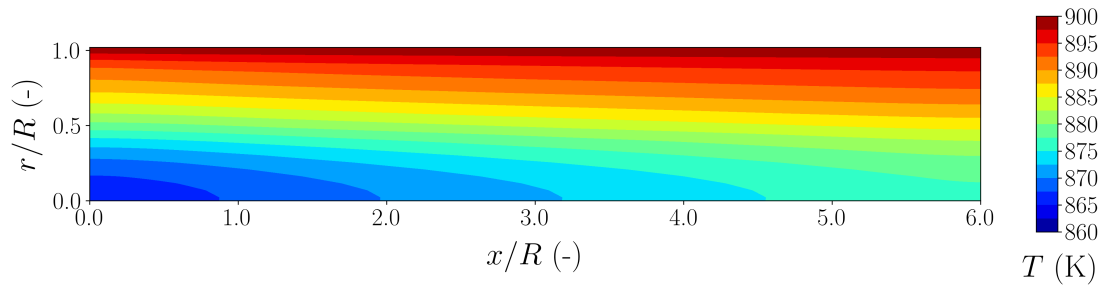


Figure 75: Strategy II - Temperature field distribution - 1<sup>st</sup> generation ( $w_{\text{CH}_4} = 0.8, w_T = 0.2, T_{\text{in}} = 900 \text{ K}, u_{\text{in}} = 0.15 \text{ m s}^{-1}, SC = 2.0$ )

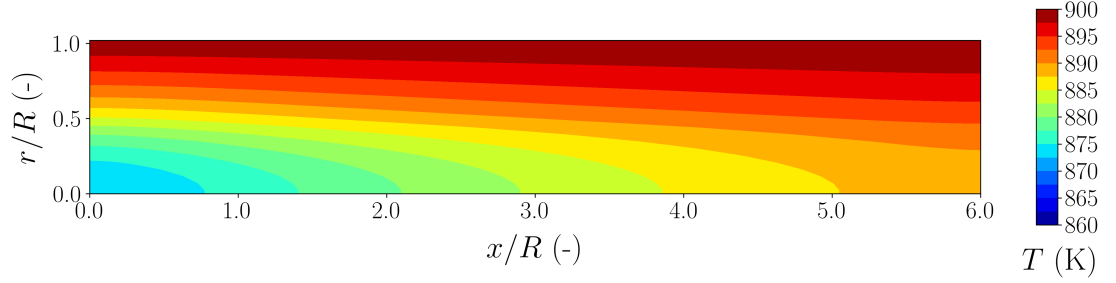


Figure 76: Strategy II - Temperature field distribution - 15<sup>th</sup> generation ( $w_{\text{CH}_4} = 0.8, w_T = 0.2, T_{\text{in}} = 900 \text{ K}, u_{\text{in}} = 0.15 \text{ m s}^{-1}, SC = 2.0$ )

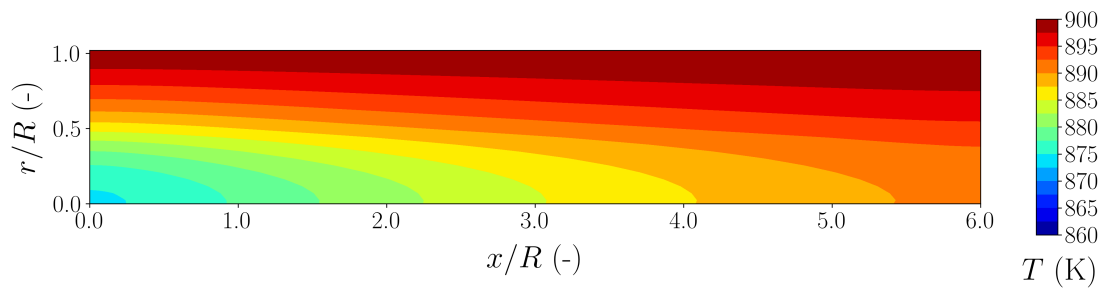


Figure 77: Strategy II - Temperature field distribution - 30<sup>th</sup> generation ( $w_{\text{CH}_4} = 0.8, w_T = 0.2, T_{\text{in}} = 900 \text{ K}, u_{\text{in}} = 0.15 \text{ m s}^{-1}, SC = 2.0$ )

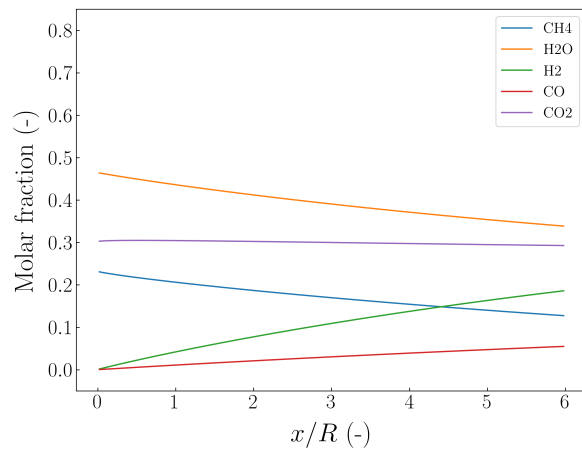


Figure 78: Strategy II - Radius-averaged molar fractions - 1<sup>st</sup> generation ( $w_{\text{CH}_4} = 0.8, w_T = 0.2, T_{\text{in}} = 900 \text{ K}, u_{\text{in}} = 0.15 \text{ m s}^{-1}, SC = 2.0$ )

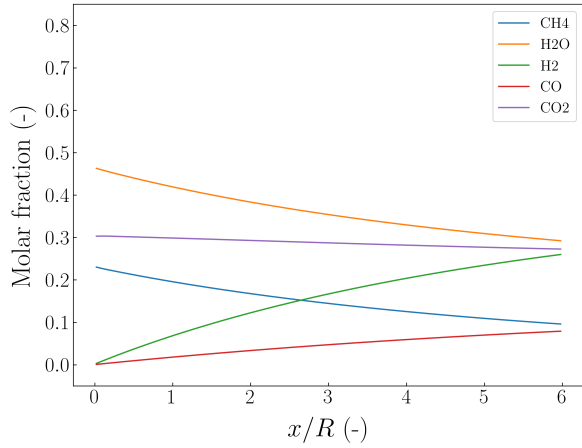


Figure 79: Strategy II - Radius-averaged molar fractions - 15<sup>th</sup> generation ( $w_{\text{CH}_4} = 0.8, w_T = 0.2, T_{\text{in}} = 900 \text{ K}, u_{\text{in}} = 0.15 \text{ m s}^{-1}, SC = 2.0$ )

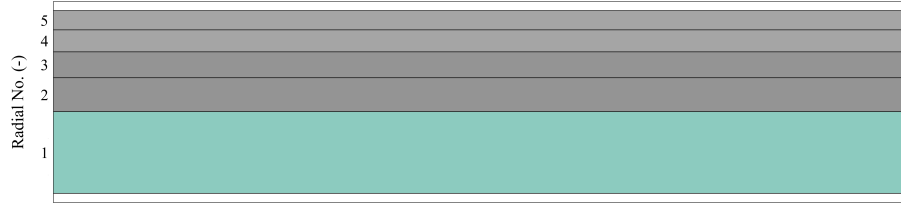


Figure 80: Strategy II - Segments distribution for 30<sup>th</sup> generation ( $w_{\text{CH}_4} = 0.8, w_T = 0.2, T_{\text{in}} = 900 \text{ K}, u_{\text{in}} = 0.15 \text{ m s}^{-1}, SC = 2.0$ )

Table 5: Hydrogen productivity for the catalytic insert division strategy II

$w_{\text{CH}_4} / w_T$	$\text{H}_{2\text{out}}$	$\iota$	$\zeta$
REF	0.581	1.00	0.581
0.2 / 0.8	0.001	0.00	N / A
0.4 / 0.6	0.492	0.32	1.527
0.5 / 0.5	0.175	0.32	0.548
0.6 / 0.4	0.536	0.53	1.616
0.8 / 0.2	0.200	0.27	0.744

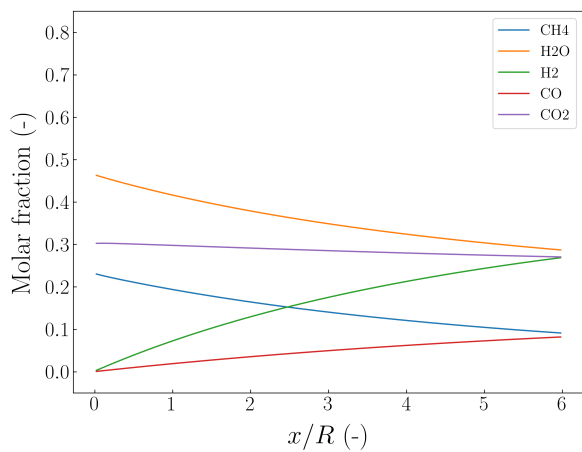


Figure 81: Strategy II - Radius-averaged molar fractions - 30<sup>th</sup> generation ( $w_{\text{CH}_4} = 0.8, w_T = 0.2, T_{\text{in}} = 900 \text{ K}, u_{\text{in}} = 0.15 \text{ m s}^{-1}, SC = 2.0$ )

## 6. Conclusions

The conducted numerical investigation regards radial segmentation of the catalyst insert. Two different configurations of coaxial segments are proposed. The radial segments may either have equal widths of the inlet surfaces or equal areas of the inlet surfaces. Each of the possible segment configurations' performance is tested against five different sets of fitness function weights. The weight sensitivity analysis is conducted to assure the best possible practices during future numerical analyses of the macro-patterned reforming reactor design optimization. Analyzing the results leads to the following conclusions:

1. Fitness weights set at 0.4 for the methane conversion and 0.6 for thermal fitness tend to deliver better results, compared with the remaining algorithms.
2. Radial segments with equal widths of the inlet surface return results of a higher quality than radial segments with equal areas of the inlet surfaces.
3. The highest values of hydrogen productivity are acquired for the reactor with equal width of inlet surfaces (Strategy IV), proving it to be the most valid approach to the optimization of the catalytic insert design.
4. The introduction of the macro-patterning concept is proven to enhance the effectiveness of the reforming reaction. The hydrogen productivity is almost tripled for the best solution when compared with the reference case.

The conducted research indicates the influence of altering the steam reforming thermal conditions on the overall process proceeding. The possible improvement of the process effectiveness on the unification of the temperature distribution is confirmed. The proposed macro-patterning concept proves the possibility of acquiring even higher methane conversion rates, using the same amount of catalyst as in the case of the reference case. However, the macro-patterned reactor would have to suffer in the compactness, as to acquire the exact level of conversion, an extension of its dimensions is required. Considering the magnitude of possible economical benefits, an enlargement to a certain extent is acceptable.

## References

- [1] U. Y. Qazi, Future of hydrogen as an alternative fuel for next-generation industrial applications; challenges and expected opportunities, *Energies* 15 (2022). URL: <https://www.mdpi.com/1996-1073/15/13/4741>. doi:10.3390/en15134741.
- [2] C. Zou, Q. Zhao, G. Zhang, B. Xiong, Energy revolution: From a fossil energy era to a new energy era, *Natural Gas Industry B* 3 (2016) 1–11. doi:<https://doi.org/10.1016/j.ngib.2016.02.001>.
- [3] G. Liobikienė, R. Dagiliūtė, Do positive aspects of renewable energy contribute to the willingness to pay more for green energy?, *Energy* 231 (2021) 120817. doi:<https://doi.org/10.1016/j.energy.2021.120817>.
- [4] H. Xu, J. Ma, P. Tan, B. Chen, Z. Wu, Y. Zhang, H. Wang, J. Xuan, M. Ni, Towards online optimisation of solid oxide fuel cell performance: Combining deep learning with multi-physics simulation, *Energy and AI* 1 (2020) 100003. URL: <https://www.sciencedirect.com/science/article/pii/S2666546820300033>. doi:<https://doi.org/10.1016/j.egyai.2020.100003>.
- [5] B. Shadidi, G. Najafi, T. Yusaf, A review of hydrogen as a fuel in internal combustion engines, *Energies* 14 (2021) 6209. doi:10.3390/en14196209.
- [6] I. Hassan, H. S. Ramadan, M. A. Saleh, D. Hissel, Hydrogen storage technologies for stationary and mobile applications: Review, analysis and perspectives, *Renewable and Sustainable Energy Reviews* 149 (2021) 111311. doi:<https://doi.org/10.1016/j.rser.2021.111311>.
- [7] C. Tarhan, M. A. Çil, A study on hydrogen, the clean energy of the future: Hydrogen storage methods, *Journal of Energy Storage* 40 (2021) 102676. URL: <https://www.sciencedirect.com/science/article/pii/S2352152X21004151>. doi:<https://doi.org/10.1016/j.est.2021.102676>.
- [8] I. Hassan, H. S. Ramadan, M. A. Saleh, D. Hissel, Hydrogen storage technologies for stationary and mobile applications: Review, analysis and perspectives, *Renewable and Sustainable Energy Reviews* 149 (2021) 111311.

- [9] M. T. Azizan, A. Aqsha, M. Ameen, A. Syuhada, H. Klaus, S. Z. Abidin, F. Sher, Catalytic reforming of oxygenated hydrocarbons for the hydrogen production: an outlook, *Biomass Conversion and Biorefinery* (2020) 1–24. doi:10.1007/s13399-020-01081-6.
- [10] R. Yukesh Kannah, S. Kavitha, Preethi, O. Parthiba Karthikeyan, G. Kumar, N. V. Dai-Viet, J. Rajesh Banu, Techno-economic assessment of various hydrogen production methods – a review, *Bioresource Technology* 319 (2021) 124175. URL: <https://www.sciencedirect.com/science/article/pii/S0960852420314498>. doi:<https://doi.org/10.1016/j.biortech.2020.124175>.
- [11] J. Chi, H. Yu, Water electrolysis based on renewable energy for hydrogen production, *Chinese Journal of Catalysis* 39 (2018) 390–394. doi:[https://doi.org/10.1016/S1872-2067\(17\)62949-8](https://doi.org/10.1016/S1872-2067(17)62949-8).
- [12] H. Zhang, Z. Sun, Y. H. Hu, Steam reforming of methane: Current states of catalyst design and process upgrading, *Renewable and Sustainable Energy Reviews* 149 (2021) 111330. URL: <https://www.sciencedirect.com/science/article/pii/S136403212100616X>. doi:<https://doi.org/10.1016/j.rser.2021.111330>.
- [13] P. Nkulikiyinka, Y. Yan, F. Güleç, V. Manovic, P. T. Clough, Prediction of sorption enhanced steam methane reforming products from machine learning based soft-sensor models, *Energy and AI* 2 (2020) 100037. URL: <https://www.sciencedirect.com/science/article/pii/S2666546820300379>. doi:<https://doi.org/10.1016/j.egyai.2020.100037>.
- [14] Z. Taherian, A. Khataee, N. Han, Y. Orooji, Hydrogen production through methane reforming processes using promoted-ni/mesoporous silica: A review, *Journal of Industrial and Engineering Chemistry* 107 (2022) 20–30. URL: <https://www.sciencedirect.com/science/article/pii/S1226086X21006675>. doi:<https://doi.org/10.1016/j.jiec.2021.12.006>.
- [15] H. H. Faheem, S. Z. Abbas, A. N. Tabish, L. Fan, F. Maqbool, A review on mathematical modelling of direct internal reforming- solid oxide fuel cells, *Journal of Power Sources* 520 (2022) 230857. URL: <https://www.sciencedirect.com/science/article/pii/S0378775321013446>. doi:<https://doi.org/10.1016/j.jpowsour.2021.230857>.

- [16] X. Zhao, B. Joseph, J. Kuhn, S. Ozcan, Biogas reforming to syngas: A review, *iScience* 23 (2020) 101082.
- [17] N. Gao, M. H. Milandile, C. Quan, L. Rundong, Critical assessment of plasma tar reforming during biomass gasification: A review on advancement in plasma technology, *Journal of Hazardous Materials* 421 (2022) 126764. URL: <https://www.sciencedirect.com/science/article/pii/S0304389421017295>. doi:<https://doi.org/10.1016/j.jhazmat.2021.126764>.
- [18] J. M. Saad, P. T. Williams, Catalytic dry reforming of waste plastics from different waste treatment plants for production of synthesis gases, *Waste Management* 58 (2016) 214–220. URL: <https://www.sciencedirect.com/science/article/pii/S0956053X16305141>. doi:<https://doi.org/10.1016/j.wasman.2016.09.011>.
- [19] B. Zhang, Y. Chen, B. Zhang, R. Peng, Q. Lu, W. Yan, B. Yu, F. Liu, J. Zhang, Cyclic performance of coke oven gas - steam reforming with assistance of steel slag derivates for high purity hydrogen production, *Renewable Energy* 184 (2022) 592–603. URL: <https://www.sciencedirect.com/science/article/pii/S0960148121017183>. doi:<https://doi.org/10.1016/j.renene.2021.11.123>.
- [20] M. Mozdzierz, G. Brus, A. Sciazko, Y. Komatsu, S. Kimijima, J. S. Szmyd, An attempt to minimize the temperature gradient along a plug-flow methane/steam reforming reactor by adopting locally controlled heating zones, *Journal of Physics: Conference Series* 530 (2014) 012040(1)–012040(8).
- [21] A. P. Simpson, A. E. Lutz, Exergy analysis of hydrogen production via steam methane reforming, *International Journal of Hydrogen Energy* 32 (2007) 4811–4820. doi:[10.1016/j.ijhydene.2007.08.025](https://doi.org/10.1016/j.ijhydene.2007.08.025).
- [22] A. T. Naseri, B. A. Peppley, J. G. Pharoah, A systematic parametric study on the effect of a catalyst coating microstructure on its performance in methane steam reforming, *International Journal of Hydrogen Energy* 40 (2015) 16086–16095. doi:[10.1016/j.ijhydene.2015.10.043](https://doi.org/10.1016/j.ijhydene.2015.10.043).
- [23] S. Ali, M. J. Al-Marri, A. G. Abdelmoneim, A. Kumar, M. M. Khader, Catalytic evaluation of nickel nanoparticles in methane steam reform-

- ing, International Journal of Hydrogen Energy 41 (2016) 22876–22885. doi:10.1016/j.ijhydene.2016.08.200.
- [24] S. T. Kolaczkowski, S. Awdry, T. Smith, D. Thomas, L. Torkuhl, R. Kolvenbach, Potential for metal foams to act as structured catalyst supports in fixed-bed reactors, Catalysis Today 273 (2016) 221–233. doi:10.1016/j.cattod.2016.03.047.
- [25] A. K. Yadav, P. D. Vaidya, Renewable hydrogen production by steam reforming of butanol over multiwalled carbon nanotube-supported catalysts, International Journal of Hydrogen Energy 44 (2019) 30014–30023. doi:10.1016/j.ijhydene.2019.09.054.
- [26] H. Butcher, C. J. Quenzel, L. Breziner, J. Mettes, B. A. Wilhite, P. Bossard, Design of an annular microchannel reactor (AMR) for hydrogen and/or syngas production via methane steam reforming, International Journal of Hydrogen Energy 39 (2014) 18046–18057. doi:10.1016/j.ijhydene.2014.04.109.
- [27] E. Meloni, M. Martino, A Short Review on Ni Based Catalysts and Related Engineering Issues for Methane Steam Reforming, Catalysts 10 (2020) 352. doi:10.3390/catal10030352.
- [28] A. Cherif, J.-S. Lee, R. Nebbali, C.-J. Lee, Novel design and multi-objective optimization of autothermal steam methane reformer to enhance hydrogen production and thermal matching, Applied Thermal Engineering 217 (2022) 119140. URL: <https://www.sciencedirect.com/science/article/pii/S1359431122010717>. doi:<https://doi.org/10.1016/j.applthermaleng.2022.119140>.
- [29] V. Palma, A. Ricca, M. Martino, E. Meloni, Innovative structured catalytic systems for methane steam reforming intensification, Chemical Engineering and Processing: Process Intensification 120 (2017) 207–215.
- [30] J. Yun, S. Yu, Transient behavior of 5 kW class shell-and-tube methane steam reformer with intermediate temperature heat source, International Journal of Heat and Mass Transfer 134 (2019) 600–609. doi:10.1016/j.ijheatmasstransfer.2019.01.078.

- [31] A. M. Dubinin, S. E. Shcheklein, V. G. Tuponogov, M. I. Ershov, Mini CHP based on the electrochemical generator and impeded fluidized bed reactor for methane steam reforming, International Journal of Hydrogen Energy 43 (2018) 13543–13549. doi:10.1016/j.ijhydene.2018.05.151.
- [32] M. Mozdzierz, G. Brus, A. Sciazko, Y. Komatsu, S. Kimijima, J. S. Szmyd, Towards a Thermal Optimization of a Methane/Steam Reforming Reactor, Flow, Turbulence and Combustion 97 (2016) 171–189.
- [33] M. Mozdzierz, M. Chalusia, S. Kimijima, J. S. Szmyd, G. Brus, An afterburner-powered methane/steam reformer for a solid oxide fuel cells application, Heat and Mass Transfer 54 (2018) 2331–2341. doi:10.1007/s00231-018-2331-5.
- [34] A. Settar, R. Nebbali, B. Madani, S. Abboudi, Numerical investigation on the wall-coated steam methane reformer improvement: Effects of catalyst layer patterns and metal foam insertion, International Journal of Hydrogen Energy 42 (2017) 1490–1498.
- [35] A. Settar, S. Abboudi, N. Lebaal, Effect of inert metal foam matrices on hydrogen production intensification of methane steam reforming process in wall-coated reformer, International Journal of Hydrogen Energy 43 (2018) 12386–12397. doi:10.1016/j.ijhydene.2018.04.215.
- [36] A. Settar, Z. Mansouri, R. Nebbali, Impact of Ni-based catalyst patterning on hydrogen production from MSR : External steam reformer modelling ScienceDirect Impact of Ni-based catalyst patterning on hydrogen production from MSR : External steam reformer modelling, International Journal of Hydrogen Energy 44 (2018) 11346–11354. doi:10.1016/j.ijhydene.2018.09.171.
- [37] M. Pajak, M. Mozdzierz, M. Chalusia, S. Kimijima, J. S. Szmyd, G. Brus, A numerical analysis of heat and mass transfer processes in a macro-patterned methane/steam reforming reactor, International Journal of Hydrogen Energy 43 (2018) 20474–20487. doi:10.1016/j.ijhydene.2018.09.058.
- [38] M. Pajak, G. Brus, J. S. Szmyd, Genetic algorithm-based strategy for the steam reformer optimization, International Journal of Hydrogen Energy (2021, In Press). doi:<https://doi.org/10.1016/j.ijhydene.2021.10.046>.

- [39] K. Boomsma, D. Poulikakos, F. Zwick, Metal foams as compact high performance heat exchangers, *Mechanics of Materials* 35 (2003) 1161–1176. doi:<https://doi.org/10.1016/j.mechmat.2003.02.001>.
- [40] A. Kaw, E. K. Kalu, D. Nguyen, *Numerical Methods with Applications*, University of South Florida, Florida, 2011.
- [41] J. Xu, G. F. Froment, Methane steam reforming: II. Diffusional limitations and reactor simulation, *AIChE Journal* 35 (1989) 97–103.
- [42] Y. Komatsu, S. Kimijima, J. S. Szmyd, A performance analysis of a solid oxide fuel cell - micro gas turbine hybrid system using biogas, *ECS Transactions* 25 (2009) 1061–1070. doi:[10.1149/1.3205631](https://doi.org/10.1149/1.3205631).
- [43] G. Brus, R. Nowak, J. S. Szmyd, Y. Komatsu, S. Kimijima, An Experimental and Theoretical Approach for the Carbon Deposition Problem During Steam Reforming of Model Biogas, *Journal of Theoretical and Applied Mechanics* 53 (2015) 273–284. doi:[10.15632/jtam-pl.53.2.273](https://doi.org/10.15632/jtam-pl.53.2.273).
- [44] M. Usman, W. Wan Daud, H. F. Abbas, Dry reforming of methane: Influence of process parameters—a review, *Renewable and Sustainable Energy Reviews* 45 (2015) 710–744. doi:<https://doi.org/10.1016/j.rser.2015.02.026>.
- [45] W. Konciewicz, M. Moździerz, G. Brus, A fast gaussian process-based method to evaluate carbon deposition during hydrocarbons reforming, *International Journal of Hydrogen Energy* (2021, In Press). doi:<https://doi.org/10.1016/j.ijhydene.2021.07.213>.
- [46] R. Kaczmarczyk, Thermodynamic analysis of the effect of green hydrogen addition to a fuel mixture on the steam methane reforming process, *Energies* 14 (2021). doi:[10.3390/en14206564](https://doi.org/10.3390/en14206564).
- [47] M. Tomiczek, R. Kaczmarczyk, M. Mozdzierz, G. Brus, A numerical analysis of heat and mass transfer during the steam reforming process of ethane, *Heat and Mass Transfer* 54 (2018) 2305–2314.
- [48] A. Mazhar, A. H. Khoja, A. K. Azad, F. Mushtaq, S. R. Naqvi, S. Shakir, M. Hassan, R. Liaquat, M. Anwar, Performance analysis of TiO<sub>2</sub>-Modified Co/MgAl<sub>2</sub>O<sub>4</sub> Catalyst for Dry Reforming of Methane in a

Fixed Bed Reactor for Syngas (H<sub>2</sub>, CO) Production, Energies 14 (2021) 3347. doi:10.3390/en14113347.

- [49] G. Brus, Y. Komatsu, S. Kimijima, J. S. Szmyd, An analysis of bio-gas reforming process on Ni/YSZ and Ni/SDC catalysts, International Journal of Thermodynamics 15 (2012) 43–51.
- [50] G. Brus, S. Kimijima, J. S. Szmyd, Experimental and numerical analysis of transport phenomena in an internal indirect fuel reforming type Solid Oxide Fuel Cells using Ni/SDC as a catalyst, Journal of Physics: Conference Series 395 (2012) 012159. doi:10.1088/1742-6596/395/1/012159.
- [51] S. Nagata, A. Momma, T. Kato, Y. Kasuga, Numerical analysis of output characteristics of tubular SOFC with internal reformer, Journal of Power Sources 101 (2001) 60–71.
- [52] K. Ahmed, K. Föger, Approach to equilibrium of the water-gas shift reaction on a Ni/zirconia anode under SOFC conditions, Journal of Power Sources 103 (2001) 150–153.
- [53] H. Iwai, Y. Yamamoto, M. Saito, H. Yoshida, Numerical simulation of intermediate-temperature direct-internal-reforming planar solid oxide fuel cell, Energy 36 (2011) 2225–2234.
- [54] A. Sciazko, Y. Komatsu, G. Brus, S. Kimijima, J. S. Szmyd, A novel approach to improve the mathematical modelling of the internal reforming process for solid oxide fuel cells using the orthogonal least squares method, International Journal of Hydrogen Energy 39 (2014) 16372–16389. doi:10.1016/j.ijhydene.2014.07.130.
- [55] X. Peng, Q. Jin, Molecular simulation of methane steam reforming reaction for hydrogen production, International Journal of Hydrogen Energy 47 (2022) 7569–7585. doi:<https://doi.org/10.1016/j.ijhydene.2021.12.105>.
- [56] G. Brus, Experimental and numerical studies on chemically reacting gas flow in the porous structure of a solid oxide fuel cells internal fuel reformer, International Journal of Hydrogen Energy 37 (2012) 17225–17234.

- [57] A. Sciazko, Y. Komatsu, G. Brus, S. Kimijima, J. S. Szmyd, An Application of Generalized Least Squares Method to an Analysis of Methane/Steam Reforming Process on a Ni/YSZ Catalyst, *ECS Transactions* **57** (2013) 2987–2996. doi:10.1149/05701.2987ecst.
- [58] A. Sciazko, Y. Komatsu, G. Brus, S. Kimijima, J. S. Szmyd, A novel approach to the experimental study on methane/steam reforming kinetics using the Orthogonal Least Squares method, *Journal of Power Sources* **262** (2014) 245–254. doi:10.1016/j.jpowsour.2014.03.097.
- [59] G. Brus, K. Miyawaki, H. Iwai, M. Saito, H. Yoshida, Tortuosity of an SOFC anode estimated from saturation currents and a mass transport model in comparison with a real micro-structure, *Solid State Ionics* **265** (2014) 13–21. doi:10.1016/j.ssi.2014.07.002.
- [60] M. Wolf, Thermodynamic assessment of the stability of bulk and nanoparticulate cobalt and nickel during dry and steam reforming of methane, *RSC advances* **11** (2021) 18187–18197.
- [61] R. G. Carbonell, S. Whitaker, Heat and Mass Transfer in Porous Media. In *Fundamentals of Transport Phenomena in Porous Media*. Editors: J. Bear, M. Y. Corapcioglu, Springer, Dordrecht, 1984.
- [62] T. Nishino, H. Komori, H. Iwai, K. Suzuki, Development of a comprehensive numerical model for analyzing a tubular-type indirect internal reforming SOFC, 1st International Fuel Cell Science, Engineering and Technology Conference Rochester, New York, USA:521-528, 2003.
- [63] T. Nishino, H. Iwai, K. Suzuki, Comprehensive Numerical Modeling and Analysis of a Cell-Based Indirect Internal Reforming Tubular SOFC, *Journal of Fuel Cell Science and Technology* **3** (2006) 33–44.
- [64] W. C. Tan, H. Iwai, M. Kishimoto, G. Brus, J. S. Szmyd, H. Yoshida, Numerical analysis on effect of aspect ratio of planar solid oxide fuel cell fueled with decomposed ammonia, *Journal of Power Sources* **384** (2018) 367–378. doi:10.1016/j.jpowsour.2018.03.011.
- [65] K. Suzuki, H. Iwai, T. Nishino, Electrochemical and thermo-fluid modeling of a tubular solid oxide fuel cell with accompanying indirect internal fuel reforming. In *Transport Phenomena in Fuel Cells*. Editors: B. Sundén, M. Faghri, WIT Press, Southampton, 2005.

- [66] B. E. Poling, J. M. Prausnitz, J. P. O'Connell, The Properties of Gases and Liquids, McGraw-Hill, New York, 2001. doi:10.1016/0894-1777(88)90021-0.
- [67] X. Yang, T. J. Lu, T. Kim, An analytical model for permeability of isotropic porous media, Physics Letters, Section A: General, Atomic and Solid State Physics 378 (2014) 2308–2311. doi:10.1016/j.physleta.2014.06.002.
- [68] A. Bhattacharya, V. V. Calmudi, R. L. Mahajan, Thermophysical properties of high porosity metal foams, International Journal of Heat and Mass Transfer 45 (2002) 1017–1031. doi:10.1016/S0017-9310(01)00220-4.
- [69] K. Boomsma, D. Poulikakos, On the effective thermal conductivity of a three-dimensionally structured fluid-saturated metal foam, Heat and Mass Transfer 44 (2001) 827–836. doi:[http://dx.doi.org/10.1016/S0017-9310\(00\)00123-X](http://dx.doi.org/10.1016/S0017-9310(00)00123-X).
- [70] Z. Dai, K. Nawaz, Y. G. Park, J. Bock, A. M. Jacobi, Correcting and extending the Boomsma-Poulikakos effective thermal conductivity model for three-dimensional, fluid-saturated metal foams, International Communications in Heat and Mass Transfer 37 (2010) 575–580. doi:10.1016/j.icheatmasstransfer.2010.01.015.
- [71] M. Pajak, S. Buchaniec, S. Kimijima, J. S. Szmyd, G. Brus, A multiobjective optimization of a catalyst distribution in a methane/steam reforming reactor using a genetic algorithm, International Journal of Hydrogen Energy 46 (2021) 20183–20197. doi:10.1016/j.ijhydene.2020.02.228.
- [72] F. Moukalled, L. Mangani, M. Darwish, The Finite Volume Method, Springer International Publishing, Cham, 2016.
- [73] S. V. Patankar, Numerical Heat Transfer and Fluid Flow, Hemisphere, Washington, 1980.
- [74] C. H. Bartholomew, Carbon deposition in steam reforming and methanation, Catalysis Reviews 24 (1982) 67–112. doi:10.1080/03602458208079650.

- [75] S. L. Lakhapatri, M. A. Abraham, Deactivation due to sulfur poisoning and carbon deposition on Rh-Ni/Al<sub>2</sub>O<sub>3</sub> catalyst during steam reforming of sulfur-doped n-hexadecane, *Applied Catalysis A: General* 364 (2009) 113–121. doi:<https://doi.org/10.1016/j.apcata.2009.05.035>.
- [76] C. Y. Zhao, Review on thermal transport in high porosity cellular metal foams with open cells, *International Journal of Heat and Mass Transfer* 55 (2012) 3618–3632. doi:[10.1016/j.ijheatmasstransfer.2012.03.017](https://doi.org/10.1016/j.ijheatmasstransfer.2012.03.017).
- [77] T. Kawashima, M. Hishinuma, Thermal properties of porous Ni/YSZ composites at high temperatures, *Materials Transactions, JIM* **37** (1996) 1518–1524.
- [78] M. J. Peet, H. S. Hasan, H. K. D. H. Bhadeshia, Prediction of thermal conductivity of steel, *International Journal of Heat and Mass Transfer* **54** (2011) 2602–2608. doi:[10.1016/j.ijheatmasstransfer.2011.01.025](https://doi.org/10.1016/j.ijheatmasstransfer.2011.01.025).
- [79] X. Y. Tai, R. Ocone, S. D. Christie, J. Xuan, Multi-objective optimisation with hybrid machine learning strategy for complex catalytic processes, *Energy and AI* 7 (2022) 100134. URL: <https://www.sciencedirect.com/science/article/pii/S266654682100080X>. doi:<https://doi.org/10.1016/j.egyai.2021.100134>.
- [80] D. E. Goldberg, *Genetic Algorithms in Search Optimization & Machine Learning*, Addison-Wesley Longman Publishing Co., Inc., Boston, 1989.
- [81] B. D. Raja, V. Patel, R. L. Jhala, Thermal design and optimization of fin-and-tube heat exchanger using heat transfer search algorithm, *Thermal Science and Engineering Progress* 4 (2017) 45–57.
- [82] J. Banhart, Manufacture, characterisation and application of cellular metals and metal foams, *Progress in Materials Science* 46 (2001) 559–632. doi:[10.1016/S0079-6425\(00\)00002-5](https://doi.org/10.1016/S0079-6425(00)00002-5).
- [83] J. Everhart, *Engineering properties of nickel and nickel alloys*, Springer Science & Business Media, 2012.
- [84] M. R. Jerrum, L. G. Valiant, V. V. Vazirani, Random generation of combinatorial structures from a uniform distribution, *Theoretical Computer Science* 43 (1986) 169–188. doi:[https://doi.org/10.1016/0304-3975\(86\)90174-X](https://doi.org/10.1016/0304-3975(86)90174-X).

- [85] M. Pajak, G. Brus, J. S. Szmyd, Catalyst distribution optimization scheme for effective green hydrogen production from biogas reforming, *Energies* 14 (2021) 5558. doi:10.3390/en14175558.
- [86] E. Zitzler, L. Thiele, Multiobjective evolutionary algorithms: a comparative case study and the strength Pareto approach, *IEEE Transactions on Evolutionary Computation* 3 (1999) 257–271. doi:10.1109/4235.797969.
- [87] A. Davahli, M. Shamsi, G. Abaei, A. Khosravi, Empirical analyses of genetic algorithm and grey wolf optimiser to improve their efficiency with a new multi-objective weighted fitness function for feature selection in machine learning classification: the roadmap, *Journal of Experimental & Theoretical Artificial Intelligence* 8 (2022) 1–36.